Mon. Not. R. Astron. Soc. **000**, 000–000 (2012) Printed 12 March 2013 (MN LaTeX style file v2.2)

arXiv:1206.1859v2 [astro-ph.CO] 11 Mar 2013

Hydrogen & Metal Line Absorption Around Low-Redshift Galaxies in Cosmological Hydrodynamic Simulations

Amanda Brady Ford[1], Benjamin D. Oppenheimer[2], Romeel Davé[1], Neal Katz[3], Juna A. Kollmeier[4], David H. Weinberg[5]

[1] *Astronomy Department, University of Arizona, Tucson, AZ 85721, USA*
[2] *Leiden Observatory, Leiden University, PO Box 9513, 2300 RA Leiden, Netherlands*
[3] *Astronomy Department, University of Massachusetts, Amherst, MA 01003, USA*
[4] *Observatories of the Carnegie Institution of Washington, Pasadena, CA 91101, USA*
[5] *Astronomy Department and CCAPP, Ohio State University, Columbus, OH 43210, USA*

12 March 2013

ABSTRACT

We study the physical conditions of the circum-galactic medium (CGM) around $z = 0.25$ galaxies as traced by H I and metal line absorption, using cosmological hydrodynamic simulations that include galactic outflows. Using lines of sight targeted at impact parameters from 10 kpc to 1 Mpc around galaxies with halo masses from $10^{11} - 10^{13} M_\odot$, we study the physical conditions and their variation with impact parameter b and line-of-sight velocity Δv in the CGM as traced by H I, Mg II, Si IV, C IV, O VI, and Ne VIII absorbers. All ions show a strong excess of absorption near galaxies compared to random lines of sight. The excess continues beyond 1 Mpc, reflecting the correlation of metal absorption with large-scale structure. Absorption is particularly enhanced within about $\Delta v < 300$ km s^{-1} and roughly 300 kpc of galaxies (with distances somewhat larger for the highest ion), approximately delineating the CGM; this range contains the majority of global metal absorption. Low ions like Mg II and Si IV predominantly arise in denser gas closer to galaxies and drop more rapidly with b, while high ions O VI and Ne VIII trace more diffusely distributed gas with a comparatively flat radial profile; C IV is intermediate. All ions predominantly trace $T \sim 10^{4-4.5} K$ photo-ionised gas at all b, but when hot CGM gas is present (mostly in larger halos), we see strong collisionally-ionised O VI and Ne VIII at $b \leqslant 100$ kpc. Larger halo masses generally produce more absorption, though overall the trends are not as strong as that with impact parameter. These findings arise using our favoured outflow scalings as expected for momentum-driven winds; with no winds, the CGM gas remains mostly unenriched, while our outflow model with a constant velocity and mass loading factor produce hotter, more widely dispersed metals.

1 INTRODUCTION

The intergalactic medium (IGM) contains most of the cosmic baryons at all epochs (e.g., Davé et al. 2001). It also contains a substantial fraction of cosmic metals (e.g., Ferrara et al. 2005; Davé & Oppenheimer 2007; Wiersma et al. 2009b), products of star formation within galaxies that have been dispersed out of galaxies presumably via large-scale galactic outflows (e.g., Aguirre et al. 2001a; Oppenheimer & Davé 2006). The distribution and physical state of these metals thus provide a powerful tracer of galactic outflow processes, which are a key uncertainty in current galaxy formation models.

Oppenheimer et al. (2012) argued from cosmological simulations with outflows that the IGM is enriched in an "outside-in" manner, with low-density regions enriched at earlier epochs, and that subsequently produced metals tend to remain closer to galaxies over the last 10 Gyr of cosmic time. In simulations by Oppenheimer & Davé (2008) that broadly reproduce IGM enrichment observations, outflowing metals reach a median distance of roughly 100 physical kpc before turning around, which is well outside the virial radius of small early galaxies but results in "halo fountains" within larger, present-day systems. Hence by low redshifts, a large fraction of the ejected metals are expected to reside close to galaxies, within what is now frequently called the circum-galactic medium (CGM). Indeed, observations indicate that C IV, Mg II and O VI absorbers can often be associated with galaxies within tens or hundreds of kpc (e.g., Steidel & Sargent 1992; Stocke et al. 2006; Wakker & Savage 2009; Prochaska et al. 2011; Chen et al. 2001; Chen & Mulchaey 2009). The CGM thus provides a fossil record of early IGM enrichment combined with the gravitational growth of structure, in addition to metals deposited by more recent outflows.

Recent observations using *Hubble's* Cosmic Origins Spectrograph (COS) provide a greatly enhanced view of CGM metals at low redshifts. Tumlinson et al. (2011)

© 2012 RAS

showed that the CGM around star-forming galaxies contains an amount of oxygen comparable to or possibly exceeding that in the interstellar medium (ISM) of those galaxies, thereby directly demonstrating that metals have been expelled *en masse* from the ISM (Tripp et al. 2011). The sensitivity of COS not only permits the selection of more numerous, fainter background sources that can probe the CGM of low-redshift galaxies, but also enables the detection of weaker and less common ions such as Ne VIII and Si IV. These data will provide new and stringent constraints on theoretical models of outflows that connect galaxies and their surrounding gas.

Cosmological hydrodynamic simulations offer a uniquely well-suited platform to study the co-evolution of galaxies and their surrounding gas. Such simulations dynamically incorporate galactic outflows driven by star formation, thereby self-consistently enriching the IGM and CGM with the by-products of stellar death, as well as accounting for the movement and physical state of such metals driven by hierarchical structure formation. With simulations of representative cosmological volumes, one can test outflow models by comparing the predicted statistics directly to absorption line observations of H I and metals, around galaxies and in the diffuse IGM. Tracking the complex inflow and outflow processes that govern both galaxies and the IGM is necessary to fully understand how IGM and CGM enrichment occur, and to properly interpret present and upcoming data with COS and other facilities.

In this paper we continue our exploration of H I and metal absorption in the low-redshift IGM using cosmological hydrodynamic simulations, building on the work presented by Davé et al. (2010) and Oppenheimer et al. (2012). In those papers we studied absorption properties along random lines of sight through cosmological volumes, which only occasionally intercepted the CGM of galaxies. In this work, we select targeted lines of sight at various impact parameters around galaxies in our simulations to directly probe the absorption properties and physical conditions of gas within the CGM. The goal of this paper is to understand the relationship between galaxy properties and HI and metal absorbers that probe the gas around those galaxies.

We explore a range of metal ionisation potential states from low (Mg II) to high (Ne VIII), as well as H I, and find that the behaviour of many CGM absorption line properties shows distinct trends with the ionisation level of the tracer species. CGM absorption lines also show trends with halo mass. These predictions set the stage for a more detailed understanding of CGM observations and provide a more complete picture for how metals trace the motion of gas in and out of galaxies.

Our paper is organised as follows: In §2 we explain our methods, in §3 we show the density and temperature of absorbers, in §4 we explore absorption around galaxies in redshift space, in §5 we study absorption as a function of impact parameter, in §6 we examine the column density distributions as a function of impact parameter and halo mass, in §7 we examine trends with outflow model, and in §8 we present our conclusions.

2 SIMULATIONS & ANALYSIS

2.1 The Code and Input Physics

We use our modified version (Oppenheimer & Davé 2008) of the N-body+smooth particle hydrodynamic (SPH) code GADGET-2 (Springel 2005), which is more fully described in §2.1 of Davé et al. (2010). The only code update since Oppenheimer & Davé (2008) is the option to include metal-line cooling rates from Wiersma et al. (2009a), as we discuss below.

Briefly, GADGET-2 computes gravitational forces on a set of particles using a tree-particle-mesh algorithm and uses an entropy-conserving formulation of SPH (Springel & Hernquist 2002) to simulate pressure forces and hydrodynamic shocks. We include radiative cooling assuming ionisation equilibrium for primordial species following Katz et al. (1996) and metals based on the tables of Wiersma et al. (2009a) that assume ionisation equilibrium in the presence of the Haardt & Madau (2001) background. In our older simulations, and our ancillary wind model simulations in this paper, we employ metal-line cooling rates based on the collisional ionisation equilibrium (CIE) models of Sutherland & Dopita (1993). The latter rates incorrectly over estimate metal-line cooling as photo-ionisation equilibrium (PIE) suppresses cooling of metal-enriched gas as demonstrated by Smith (2011) and Tepper-García et al. (2011). We show comparisons of these two cooling models in §7.

Star formation follows a Schmidt (1959) Law calibrated to the Kennicutt (1998) relation, following Springel & Hernquist (2003). The interstellar medium (ISM) is modelled using the analytic sub grid recipe of McKee & Ostriker (1977), where supernova energy is returned to ISM particles using the two-phase SPH formulation of Springel & Hernquist (2003). Star particles are spawned from ISM particles probabilistically according to the instantaneously calculated star formation rate (SFR); an ISM particle can spawn up to two star particles.

Star formation-driven kinetic feedback is implemented in these simulations by giving a velocity kick ($v_{\rm w}$) to ISM particles chosen probabilistically at a rate proportional to their star formation rate. The ratio of the mass outflow rate to the star formation rate is termed the mass loading factor (η). We use the relations for $v_{\rm w}$ and η of momentum-driven winds formulated by Murray et al. (2005):

$$\begin{aligned} v_{\rm w} &= 3\sigma\sqrt{{\rm f}_L - 1} \qquad (1)\\ \eta &= \sigma_o/\sigma, \qquad (2) \end{aligned}$$

where $\rm f_L$ is the luminosity in units of the Eddington luminosity required to expel gas from a galaxy potential, $\sigma_o = 150\ {\rm km\,s^{-1}}$, and σ is the galaxy's internal velocity dispersion (Oppenheimer & Davé 2008). We refer to this wind model as "vzw" and refer the reader to Oppenheimer & Davé (2008) for a more complete description. We also evolve a model without winds ("nw") and a constant wind ("cw") model with $v_{\rm w} = 680\ {\rm km\,s^{-1}}$ and $\eta = 2$ for all galaxies, as described in Davé et al. (2010).

Table 1. Comparison of r48n384vzw models.

Z-Cooling	CIE[a]	PIE[b]
$f_{\rm bar}(T \geqslant 10^5{\rm K})$[c]	0.394	0.408
$f_{\rm metals}(T \geqslant 10^5{\rm K})$[d]	0.056	0.066
Ω_*/Ω_b[e]	0.084	0.076
ρ_{SFR}[f]	0.074	0.066
${\rm dN/dz}(N_{\rm H\,I} \geqslant 10^{14}{\rm cm}^{-2})$[g]	8.88	7.94
$\Omega_{\rm OVI}$[h]	57.6	38.8
$\Omega_{\rm CIV}$[h]	33.9	23.7
$\Omega_{\rm SiIV}$[h]	10.2	7.9

[a] Collisional ionisation equilibrium metal cooling rates from Sutherland & Dopita (1993).

[b] Photo-ionisation equilibrium metal cooling rates using Wiersma et al. (2009a).

[c] Fraction of diffuse, non-ISM baryons with $T \geqslant 10^5$ K at $z = 0.25$.

[d] Fraction of diffuse, non-ISM metals with $T \geqslant 10^5$ K at $z = 0.25$.

[e] Fraction of baryons in stars at $z = 0.25$.

[f] Instantaneous SFR at $z = 0.25$ in $M_\odot$ yr^{-1} Mpc^{-3}

[g] Frequency of H I components with $N_{\rm H\,I} \geqslant 10^{14}{\rm cm}^{-2}$ at $z = 0.25$.

[h] Ω summed from all gas outside galaxies at $z = 0.25$, in units of 10^{-8}.

2.2 Simulation Runs

Our main model in this paper is a $48h^{-1}$Mpc, 2×384^3 simulation with vzw winds. This simulation is identical to the r48n384vzw simulation used by Oppenheimer et al. (2010, 2012) and Davé et al. (2010, 2011a,b) except that it uses Wiersma et al. (2009a) metal-line cooling rates.

We choose the vzw wind model as our fiducial model owing to its successes fitting important properties of galaxies and the IGM at a variety of redshifts. At high redshift, simulations with vzw winds provide adequate fits to the $z = 2$ mass-metallicity relationship (Finlator et al. 2008; Davé et al. 2011a), the $z \geqslant 6$ galaxy luminosity function (Davé & Oppenheimer 2007; Finlator et al. 2011), and observations of IGM metal enrichment at redshifts $\geqslant 1.5$ (Oppenheimer & Davé 2006; Oppenheimer et al. 2009). Simulations evolved to $z = 0$ reproduce the observed galactic stellar mass function (Bell et al. 2003; Baldry, Glazebrook, & Driver 2008) below 5×10^{10} $M_\odot$ (Oppenheimer et al. 2010), various statistical properties of present-day galaxies (Davé et al. 2011a,b), and H I and metal-line statistics from quasar absorption line (QAL) spectra (Oppenheimer & Davé 2009; Oppenheimer et al. 2012). Oppenheimer et al. (2012) explored a small, $16h^{-1}$Mpc, 2×128^3 simulation incorporating vzw winds and Wiersma et al. (2009a) metal-line cooling, finding it to be their preferred model owing to its theoretically motivated feedback prescription capable of reproducing the above-listed observations, combined with a more correct treatment of metal-line cooling. Oppenheimer et al. (2012) also compared the vzw model, as well as a constant wind and no wind model, to observations of random lines of sight, as shown in Figures 6-8, 10, 14-15, 18 and 21. We note that these simulations do not include any additional mechanisms such as black hole feedback to quench star formation in massive galaxies to reproduce the observed galaxy red sequence (e.g., Gabor et al. 2011).

Because the old r48n384vzw evolved with CIE cooling was featured prominently in a number of our previous publications (Oppenheimer et al. 2010; Davé et al. 2010, 2011a,b; Oppenheimer et al. 2012), we list the differences in some relevant quantities relative to using PIE cooling rates in Table 1 at $z = 0.25$. It shows that the differences that result from replacing CIE with PIE metal-line cooling rates are minor to moderate. The fraction of baryons in diffuse (i.e. non-star forming) gas with $T \geqslant 10^5$ K increases by 3.6%, while the associated metals increase by 18%. Less cooling allows more baryons and especially metals to remain in the warm-hot intergalactic medium (WHIM), defined as where $T > 10^5$ K and $\delta < \delta_{th}$, where δ_{th} is the division between bound and unbound gas (Oppenheimer et al. 2012; Davé et al. 2010). The total integrated star formation (i.e. baryon fraction in stars) is reduced by 10%, and the instantaneous star formation rate is reduced by 11%, both because enriched winds are less capable of cooling and hence recycling onto galaxies (Oppenheimer et al. 2010). Considering Lyα absorption tracing the IGM, the frequency of single Voigt-profile-fitted components with $N_{\rm H\,I} \geqslant 10^{14}{\rm cm}^{-2}$ drops by 10.6%. Common metal ion species observed by COS all decline by 23-33%, which was also found by Oppenheimer et al. (2012) and shown to provide as good if not better agreement with the available observations. Hydrogen and metal-line absorption primarily arise from $T < 10^5$ K gas, which is reduced with PIE cooling, and more so for metals. The relative differences between these two vzw simulations using CIE or PIE metal cooling is less than it would be for a stronger wind model such as that used in Wiersma et al. (2009a), because with vzw winds diffuse metals are placed at higher overdensities where they cool rapidly in either cooling scheme (Oppenheimer et al. 2012).

In §7, we compare these vzw wind models to two other wind models, a constant wind and a no wind model, both with $48h^{-1}$Mpc size and 2×384^3 resolution. The constant wind model presented here has Wiersma et al. (2009a) metal-line cooling, included because Oppenheimer et al. (2012) found that PIE cooling was more important for metals pushed to lower densities by these stronger winds. We use the same no wind simulation as in Oppenheimer et al. (2010). Since metals rarely reach densities where PIE metal cooling is important, there is no need to rerun a no wind simulations with PIE metal cooling.

Finally, the cosmology used in our r-series simulations is: $\Omega_{\rm m} = 0.28$, $\Omega_\Lambda = 0.72$, $h = 0.7$, spectral index $n = 0.96$, $\sigma_8 = 0.82$, and $\Omega_{\rm b} = 0.046$. This agrees with the WMAP-7 constraints (Jarosik et al. 2011). The gas particle mass is 3.56×10^7 M$_\odot$, and the dark matter particle mass is 1.81×10^8M$_\odot$ giving an effective galaxy mass resolution of about 2.3×10^9M$_\odot$ and a dark matter halo mass resolution of about 1.21×10^{10}M$_\odot$. In this paper we will focus on galaxies and halos generally well above these resolution limits. Unless otherwise specified, we quote distances in physical (not comoving) units, and we usually refer to them in Mpc rather than h^{-1} Mpc.

2.3 Generating Spectra with Specexbin

We use our spectral generation code Specexbin to calculate physical properties of the gas. Specexbin is described in more detail in §2.5 of Oppenheimer & Davé (2006) and more recently in §2.3 of Davé et al. (2010). Briefly, Specexbin averages physical properties including the gas density, the temperature, the metallicity and the velocity of SPH particles in physical coordinates along a sight line. It then uses look-up tables calculated with CLOUDY (Ferland et al. 1998, version 08.00) to find the ionisation fraction for the relevant ionic species.

These look-up tables, functions of density, temperature, and redshift, have been calculated assuming collisional plus photo-ionisation equilibrium with a uniform Haardt & Madau (2001) background. SPECEXBIN then converts to velocity coordinates using Hubble's Law, accounting for the peculiar velocities of the SPH particles, and adds thermal broadening using the temperature and atomic weights of the various ion species. To match the mean observed absorption we multiply the Haardt & Madau (2001) spectrum by factors of 1.5 for the vzw model, and 1.11 for the no wind and constant wind models, as found in Davé et al. (2010).

Since our last published work with SPECEXBIN, we have updated the code to include an approximate physically motivated self-shielding from the ionisation background. This is significant here owing to the fact that we are interested in absorption close to galaxies that may arise in fairly dense (and possibly self-shielded) gas. The self-shielding correction is purely local and is done on a particle-by-particle basis. We compute the fraction of each particle's mass that is internally self-shielded from the ionising background by integrating the H I column density inwards from the particle's edge, assuming that it has a density profile given by the SPH smoothing kernel, until the column density crosses a threshold; within that radius we assume that all the hydrogen is neutral. We choose a threshold of 10^{18}cm^{-2}, which provides the best fit to the neutral fractions obtained in the full radiative transfer models of Faucher-Giguère et al. (2009). In practise, because of a reasonably tight correlation between column density and physical density (e.g., Davé et al. 2010), this results in a fairly sharp density threshold of 0.01 cm^{-3} above which the gas is fully neutral. If the gas density is greater than 0.13 cm^{-3} our star formation algorithm assumes that it is star-forming. In this case we assume that the gas is completely neutral, which is reasonable since the cold fraction in the two-phase medium always dominates by mass over the hot fraction. This choice of self-shielding correction also moves all the magnesium into Mg II, which is what one expects for magnesium in neutral hydrogen based upon the ionisation potentials of magnesium. For random sight lines, we rarely probe these densities, but for targeted lines of sight particularly within 10 kpc of a galaxy, the effects of self-shielding can be significant. We also put in a transition from neutral to molecular HI for ISM gas using the Blitz & Rosolowsky (2006) pressure criterion.

Our spectral extraction implicitly assumes that all metals are in the gas phase, but the observed correlation of quasar colours with projected separation from foreground galaxies suggests substantial amounts of intergalactic dust (Ménard et al. 2010). Zu et al. (2011) show that our vzw simulations can reproduce the Ménard et al. (2010) observations if roughly 25% of extragalactic metals (by mass) are depleted onto dust with an SMC-like grain size distribution. Precise accounting is difficult because of uncertainties in the observations, in the composition and size distribution of the dust grains, and in the destruction and production rates as a function of time and galactocentric distance. Dust depletion is an inevitable source of uncertainty in metal-line absorption predictions from cosmological simulations; it could plausibly lower our predicted absorption for refractory elements such as carbon and silicon by 25-50%.

2.4 Ion Selection

We investigate six different species: H I1216, Mg II2796, Si IV1394, C IV1548, O VI1032, and Ne VIII770. These represent some of the most common metal ions that COS probes, along with H I. All the metal lines have doublets, making their identification in observed spectra more straightforward. While H I in the Lyα forest is associated with diffuse baryons tracing large-scale structures in the Universe (e.g., Davé et al. 1999), stronger H I absorbers are associated with higher-density structures in the CGM (e.g., Fumagalli et al. 2011; van de Voort 2011) and are sensitive to the outflow model used in the simulation (e.g., Davé et al. 2010) as well as the cooling implementation (see Table 1).

Mg II is one of the most common observed lines in QAL spectra, and it appears to be associated with the CGM environments of galaxies, especially star-forming ones (e.g., Kacprzak et al. 2007), and may indicate recent outflows (e.g., Bordoloi et al. 2011; Bouche et al. 2012; Matejek & Simcoe 2012) and/or inflowing gas (Kacprzak et al. 2010). Mg II is often associated with H I absorbers of $N_{\rm H\,I} = 10^{16.5} - 10^{21.0}$cm^{-2} (e.g., Hellsten et al. 1998), indicating that Mg II frequently arises from self-shielded gas. Since our cosmological simulations do not have the resolution to fully resolve this self-shielding, we make the assumption that all magnesium in a self-shielded region is Mg II, because the ionisation potential of Mg II is above the H I ionisation energy while Mg I is below it. We cannot resolve the true substructure of Mg II, but we hope to understand the typical densities and environments from which this absorption arises. This prescription produces equivalent widths that roughly match recent observations by Rubin et al. (2012), suggesting that our Mg II modelling is not dramatically wrong.

Si IV and C IV are relatively strong lines that fall within the far-UV window often probed by COS. These are mid-ionisation potential lines that typically arise in optically thin gas, but still probe fairly overdense regions at low redshifts (Oppenheimer et al. 2012).

O VI is the most commonly observed high ionisation potential metal absorber at low redshifts (e.g., Tumlinson et al. 2011; Danforth & Shull 2008; Thom & Chen 2008; Bregman 2007; Stocke et al. 2006; Chen & Mulchaey 2009; Prochaska et al. 2011; Sembach et al. 2003; Tripp et al. 2000, 2008). Oppenheimer & Davé (2009) examined the nature of diffuse O VI absorbers in these simulations using random lines of sight through their simulation volume and found that it traces mostly photo-ionised gas in the diffuse IGM, warm-hot gas, and gas within halos. Here we focus on O VI absorption within halo gas, which we will compare to the previous results from Oppenheimer et al. (2012) on diffuse IGM O VI.

The highest ionisation potential line that we consider is Ne VIII, and it is valuable because it can trace 10^{5-6} K gas (Savage et al. 2005) better than any other UV resonance line. Nonetheless, as argued in Oppenheimer et al. (2012), very weak Ne VIII can arise in gas photo-ionised by the metagalactic background. Recent observations of Ne VIII by Tripp et al. (2011) and Mulchaey & Chen (2009) have been interpreted to suggest that Ne VIII absorption arises from a transitional phase on the surfaces of cold clouds moving through hotter material. Unfortunately, our simulations are not able to resolve such surfaces, so we may be missing this component of Ne VIII absorption in our models. Nonetheless, we do find a significant number of such absorbers, in rough agreement with data (Oppenheimer et al. 2012).

2.5 Generating and Analysing Simulated Spectra

We examine both targeted and random lines of sight (LOS). For our targeted LOS we randomly select central galaxies for each of three different halo mass bins: $10^{10.75-11.25}$ M$_\odot$ (labelled 10^{11} M$_\odot$) ; $10^{11.75-12.25}$ M$_\odot$ (labelled 10^{12} M$_\odot$) and $10^{12.75-13.25}$ M$_\odot$ (labelled 10^{13} M$_\odot$). For $10^{11}M_\odot$ and $10^{12}M_\odot$, we select 250 galaxies, while for $10^{13}M_\odot$ there are only 86 central galaxies in the simulation so we use all of them in our sample. Because we do not properly model the detailed internal structure of the ISM in our galaxies, we do not present results through the centres of the galaxies, but rather start at $b = 10$ kpc. We choose impact parameters b ranging from 10 kpc (centre) out to 1 Mpc, with the spacing increasing with b. For each impact parameter b, we produce four LOS per galaxy, meaning x+b, x-b, y+b, y-b, for a total of 1,000 LOS per b per mass bin (344 for $10^{13}M_\odot$).

We also generate random LOS, to compare with our targeted LOS. For our random LOS, we choose a 100×100 grid spanning the simulation in $x - y$ space, for a total of 10,000 LOS. These are similar to the spectra generated for Oppenheimer et al. (2012).

After generating optical depths with SPECEXBIN, we construct artificial spectra by convolving our data with COS's line spread function (LSF) and adding Gaussian random noise with S/N=30 per 6 km s^{-1} pixel. The LSF is roughly Gaussian with a ≈ 17 km/s FWHM, but it has some non-Gaussianity in the wings. Also, there is a small wavelength dependence to the LSF; for simplicity, we choose the G130M LSF at 1450Å as representative of all wavelengths to avoid complications in our interpretations owing to variations in the LSF.

Figure 1 shows examples of our simulated spectra. For each column, a single central galaxy is chosen from that mass bin, and we plot spectra at impact parameters of 10 kpc (red), 100 kpc (green), and 1 Mpc (blue) away from that galaxy. These particular galaxies were chosen for this figure since they have many absorption features, which illustrates the methodology well, although that is not necessarily typical.

The top two panels show the gas temperature and density weighted by H I optical depth, and the lower panels show simulated spectra for H I and other ions as labelled. As expected, the gas density is higher at smaller impact parameters, which yields stronger absorption in most ions. Also, more massive halos generally have more absorption. While this figure only shows three selected galaxies, one can already see some of the trends that will be explored and quantified later in this paper, although other trends are statistical in nature and not well depicted in this figure.

We fit Voigt profiles to the absorption features using AUTOVP (Davé et al. 1997), which yields column densities, line widths, (rest) equivalent widths, and redshifts for each absorber. We set the detection significance criterion to 4σ, which should be quite conservative given that the noise is Gaussian random by construction. Since the details of deblending absorption features into multiple components can be quite sensitive to the noise level and algorithmic details, we generally focus on absorption *systems*, in which we combine all lines that have separations $<$ 100 km/s. This mitigates the sensitivity to these issues, and allows for a more robust comparison to the observations, at the cost of discarding some of the information available about the internal kinematics of the absorption features. Some of our figures below plot median line properties, and since weak lines outnumber strong lines, median properties necessarily depend on the lower cutoff. Our results should be taken to refer to the population of lines detectable with typical S/N=30 COS spectra, with closely separated components combined into systems.

3 PHYSICAL CONDITIONS OF ABSORBERS

3.1 The CGM in Absorption

We seek to understand the density and temperature of the CGM and how those conditions give rise to the presence of various observable ions. We begin by presenting a pictorial overview of the simulated CGM, as seen in physical conditions and line absorption, to build our intuition as to how these physical conditions relate to observables.

Figure 2 shows a stacked median image of the galaxies around which we generate our targeted lines of sight. We generate the images by taking the pixel-by-pixel median of each given quantity for the 250 galaxies in the mass bin of $10^{11}M_\odot$ (top row) and $10^{12}M_\odot$ (middle row), and the 86 galaxies in the $10^{13}M_\odot$ mass bin (bottom row). Because this is a pixelized median, the satellites are effectively removed. The depth of the image is 658 kpc centred at the redshift of the galaxy ($\approx$ 1.2% of the full simulation depth). The first two columns show the median overdensity and median temperature of all the gas. The remaining plots show, in each column, the absorption in the various ions that we consider in this paper, again for each of our three halo mass bins. Note the colour scale for HI, subdividing H I into damped Lymanα systems(red), Lyman-limits sytems (green) and the Lyα forest (blue), consistent with Pontzen et al. (2008) and van de Voort et al. (2012), is different from the metal lines. We also include, in the lower two panels, results for two different wind models, a constant wind "cw" model and a no wind "nw" model for the $10^{12}M_\odot$ halo mass bin (see §7).

As expected, the gas density is strongly concentrated towards the (stacked) central galaxy. Galaxies in more massive halos have a larger extent. The temperatures increase with mass bin, with the $10^{13}M_\odot$ mass bin showing halo gas that is predominantly near the virial temperature, but other halos showing more sub-virial temperatures. This reflects the now well-understood division at $10^{12}M_\odot$ between cold and hot-gas-dominated halos (e.g., Kereš et al. 2005; Dekel & Birnboim 2006; Gabor et al. 2011). Some cool gas must be present in $10^{13}M_\odot$ mass halos, however, since we

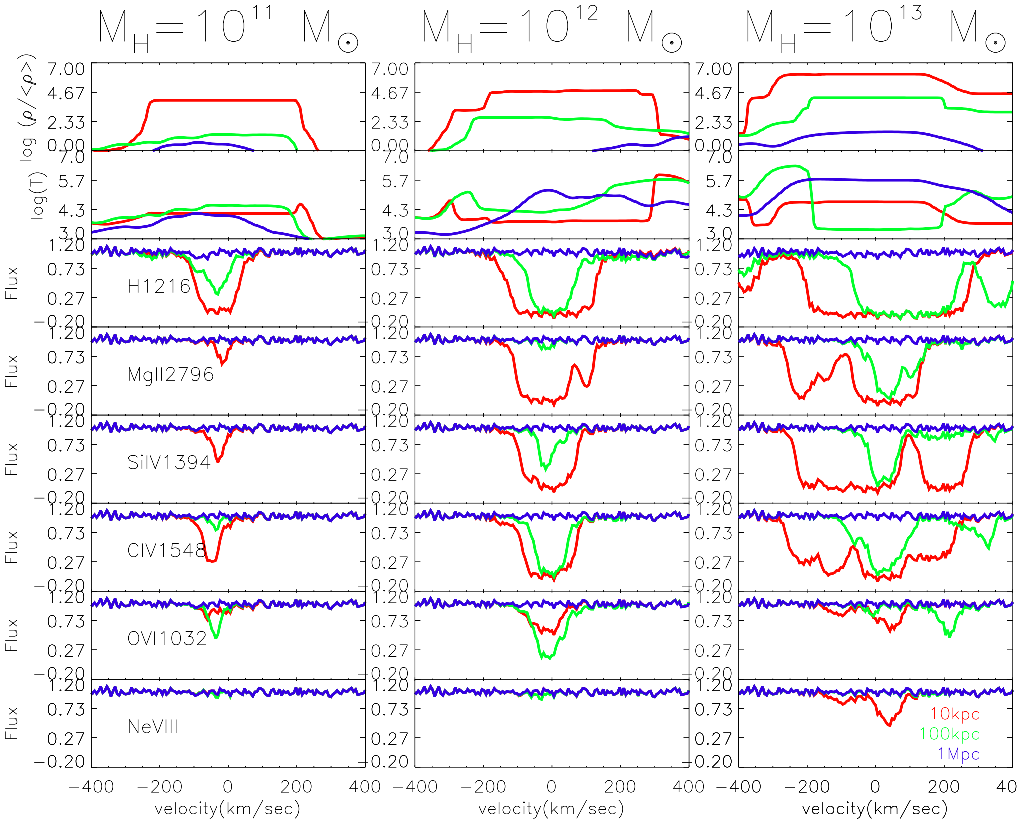

Figure 1. Simulated spectra for three galaxies at z=0.25, convolved with the COS line spread function and noise added with a S/N=30. Each column corresponds to a representative galaxy with the labelled halo mass. We plot lines of sight at distances of 10 kpc (red), 100 kpc (green), and 1 Mpc (blue) away from the galaxy. The top two panels show the H I optical depth-weighted density and temperature, and the lower panels show simulated spectra for H I and other ions. All units are physical, for a Hubble parameter $h = 0.7$.

find significant H I absorption (see §3.4). We reiterate that our simulations do not include a prescription to quench star formation in hot halos, which is required to produce red and dead galaxies (Gabor et al. 2011), so more realistic models might have less cool gas in $10^{13}M_\odot$ halos. However, recent observations (Thom et al. 2012, in preparation), suggest that even early type galaxies have prevalent H I absorption, so perhaps whatever mechanism quenches star formation does not greatly impact the cooler halo gas.

The morphology of the absorption (neglecting individual satellite contributions) is strongly dependent on the ion being probed. Mg II is highly centrally concentrated, and shows very little qualitative morphological difference between the different halo masses (on this plot scale). At the opposite extreme, Ne VIII shows very diffuse, extended absorption in the lower mass halos, and is more centrally concentrated in the highest halo mass bin. The other ions lie in between these two extremes, progressing smoothly through Si IV, C IV, and O VI. We foreshadow our upcoming results by ordering these ions by increasing ionisation potential, which we will demonstrate provides an intuitive guide towards understanding how absorption traces physical conditions.

3.2 Phase Space Plots

To begin to quantify the physical conditions giving rise to H I and metal absorption around galaxies, it is useful to examine the location of absorption systems in density-temperature phase space. This provides a valuable overview of the physical conditions of the gas traced by the various absorption species and sets the stage for discussing how various observable properties trace these underlying physical conditions. We thus begin by examining where our systems appear in phase space as a function of impact parameter.

In Figures 3–5 we show the overdensity-temperature space locations of absorption systems (circles, colour-coded by column density) at different impact radii as labelled, overlaid on the global (i.e. cosmic) mass distribution of that ion ($\Omega_{\rm ion}$) computed for all non star-forming gas ($n_H < 0.13$ cm^{-3}) in the simulation volume (grey shading). We plot this for galaxies in our 10^{12} $M_\odot$ halo mass bin. The vertical dashed line shows the cosmic mean density at $z = 0.25$ ($n_{\rm H} = 10^{-6.43}$ cm^{-3}), and the solid horizontal and vertical lines subdivide this cosmic phase space into the four regions defined by Davé et al. (2010). The temperature cut at $T = 10^5$ K divides "hot" phases from "cool" phases, and the density cut distinguishes halo gas ($n_{\rm H} > 10^{-4.47}$ cm^{-3}, i.e. the virial radius density at $z = 0.25$) from diffuse, intergalactic gas. The four quadrants, going clockwise starting at the

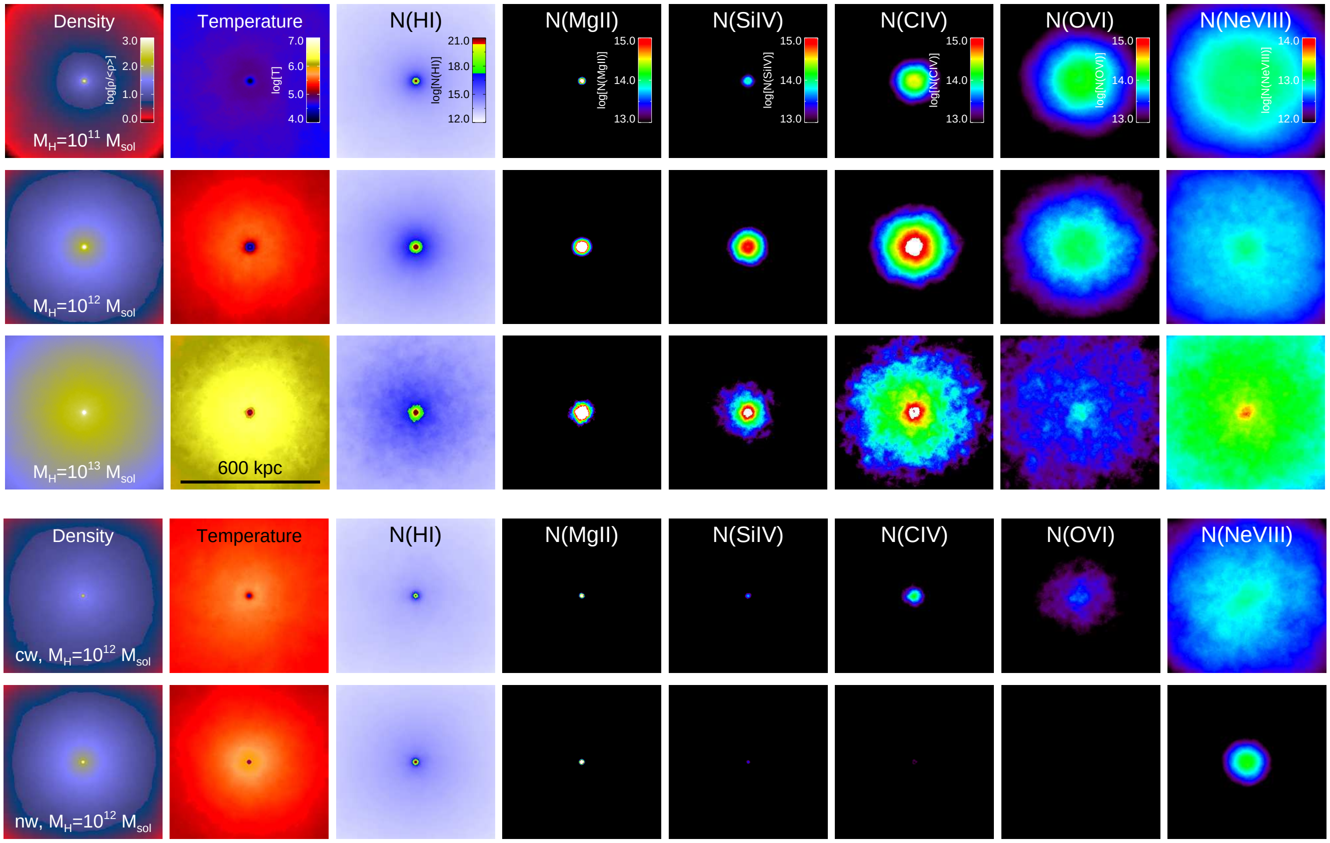

Figure 2. Columns one and two show the median log overdensity and median log temperature; subsequent columns show median log column densities for each ion as labelled, all at z=0.25. First three rows are for vzw; the first row is for mass bin $10^{11}M_{\odot}$, second for $10^{12}M_{\odot}$, and the third for $10^{13}M_{\odot}$. The fourth and fifth rows are for $10^{12}M_{\odot}$ halos in the constant wind and no wind models, respectively, and are discussed further in §7. Note the colour scales for H I and Ne VIII are different than for the other ions. All panels are 658 kpc across.

upper right, therefore, correspond to: hot halo, condensed, diffuse, and WHIM gas.

In targeted sight lines, components found within ± 300 km s^{-1} of the targeted galaxy are considered to be associated with the galaxy (as described further in §4). Those components are then grouped into systems. Our definition of a system is all the components that lie within 100 km s^{-1} of any other component within that system. We do this because fitting detailed line profiles can be non-unique and quite sensitive to the assumed S/N, as described further in §2.5. The temperatures and densities of the systems are calculated as the column density-weighted means of the individual components. In most cases, a single component dominates a system.

The histograms along the temperature and overdensity axes indicate the relative fractions of the cosmic mass density (grey histograms) and the absorption systems found in our lines of sight (red) as a function of temperature and overdensity. Comparing the red and grey histograms indicates how well the absorption seen in each ion at a given impact parameter traces the underlying density and temperature distribution of all such ions within the volume. Note that the histograms are linearly (not logarithmically) scaled, and that the integral under the red and grey histograms are set to be equal. The grey histograms are the same for all plots of a given ion, and sum only gas outside galactic ISM. In contrast, the red histograms vary depending on the absorption found for the targeted sight lines at various b. To avoid outliers dominating the computation, the red histograms have been generated with a cap in column density of 10^{16} cm^{-2} for H I and 10^{15} cm^{-2} for the metal lines. All the lines above these values have been set to this value when summing the column density-weighted histogram, to avoid having the histograms skewed by single large, saturated absorbers, since such absorbers generally have highly uncertain column densities from Voigt profile fitting. This affects 1.3% of all H I absorbers and no more than 0.7% of all metal-line systems.

The vertical column of panels show the distribution at three different targeted impact parameters, 10 kpc, 100 kpc, and 1 Mpc, along with random LOS (bottom) for each ionic species. The different columns correspond to different ions, beginning with H I and then ordered by increasing ionisation potential (discussed below in Figure 6), namely Mg II, Si IV, C IV, O VI, and Ne VIII. Each galaxy has four LOS per impact parameter, and there are 250 galaxies per mass bin. Therefore, each panel of the top three rows represent 1000 lines of sight. We use a velocity window of ± 300 km s^{-1} for the targeted LOS throughout, which we explain in §4 as the rough window containing the majority of absorption associated with the galaxy. Hence, the total path length in each panel is 6×10^5 km s^{-1} or $\delta z = 2.52$. In the bottom row,

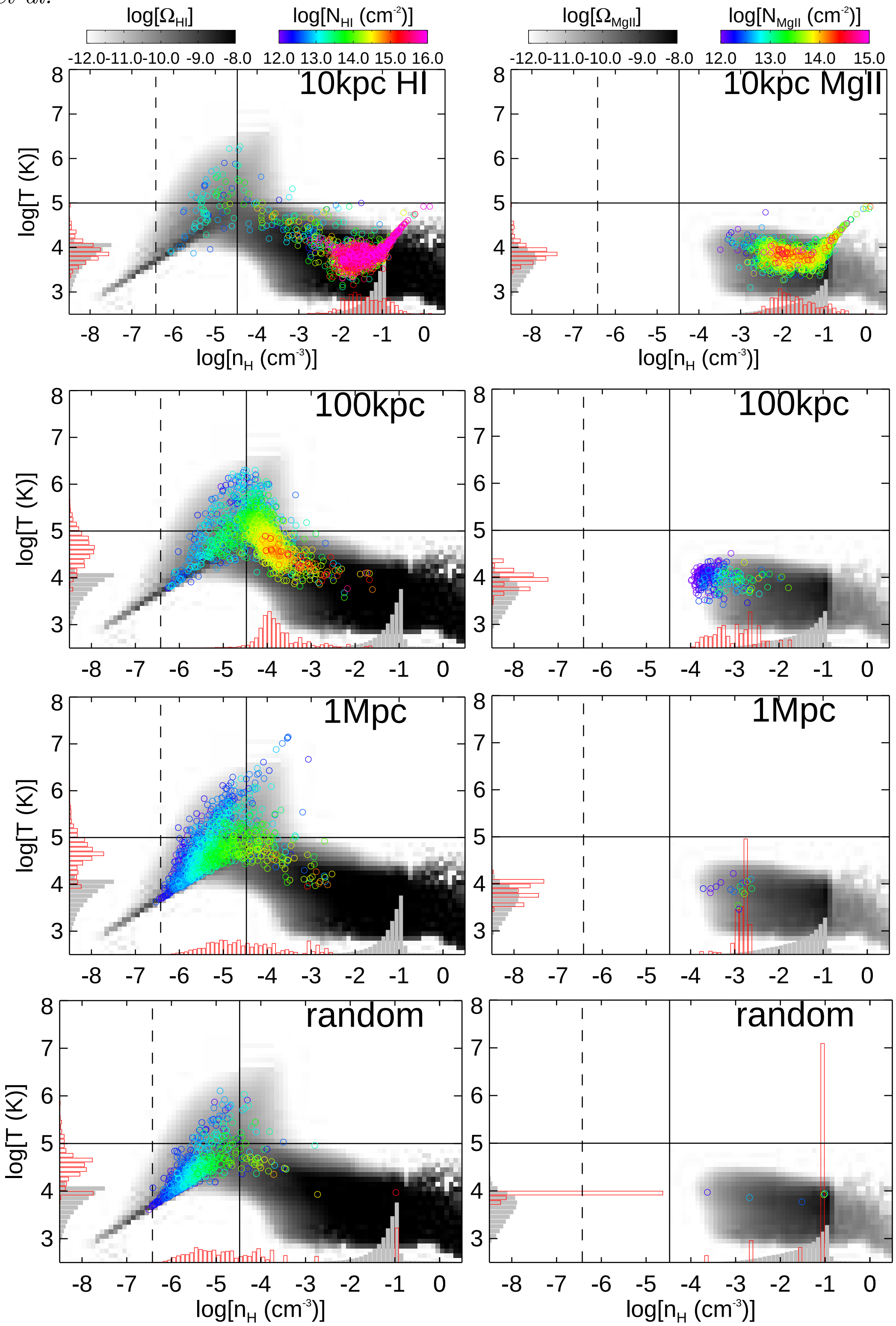

Figure 3. Phase space plots showing the location, in density and temperature space, of H I (left) and Mg II (right) for $M_h = 10^{12}\ M_\odot$ at z=0.25. Each coloured point represents an absorption system found along targeted lines of sight at 10 kpc (top row), 100 kpc (second), 1 Mpc (third), and along random lines of sight (bottom). The grey shading shows the mass-weighted absorption for all gas below $n_H = 0.13$ cm^{-3} outside of all galaxies in the simulation volume, at each location in phase space. This is identical in each plot of a given ion. The red and grey histograms show the distributions in identified absorbers and the entire volume, respectively, collapsed along each axis. The histograms are linearly scaled, and the integral under the red and grey histograms are set to be equal. Note that the absorber colour scale is different for H I.

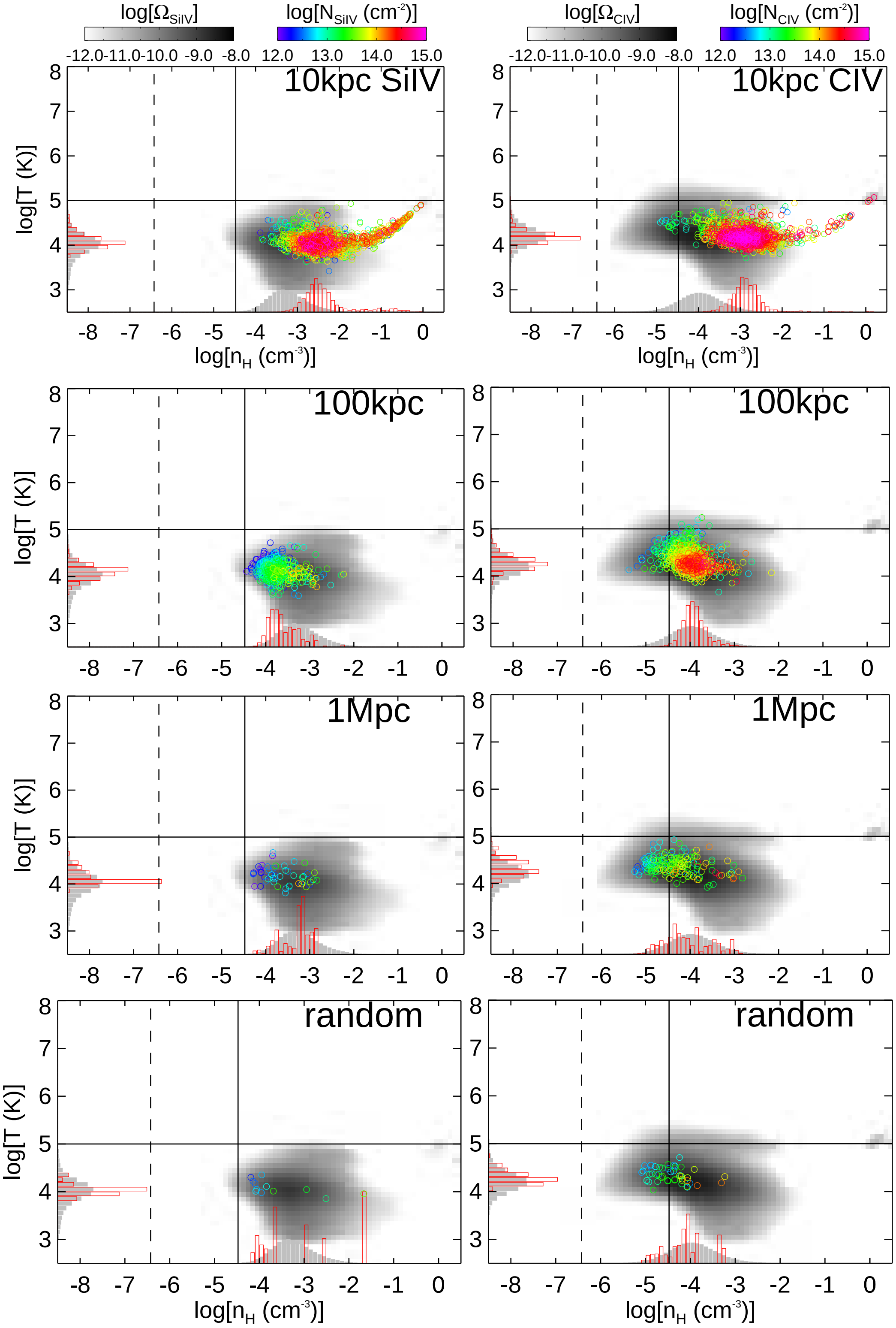

Figure 4. Analogous to Figure 3, phase space plots showing the location, in density and temperature space, of Si IV (left) and C IV (right) absorbers, for $M_h = 10^{12}\ M_\odot$, at the impact parameters indicated.

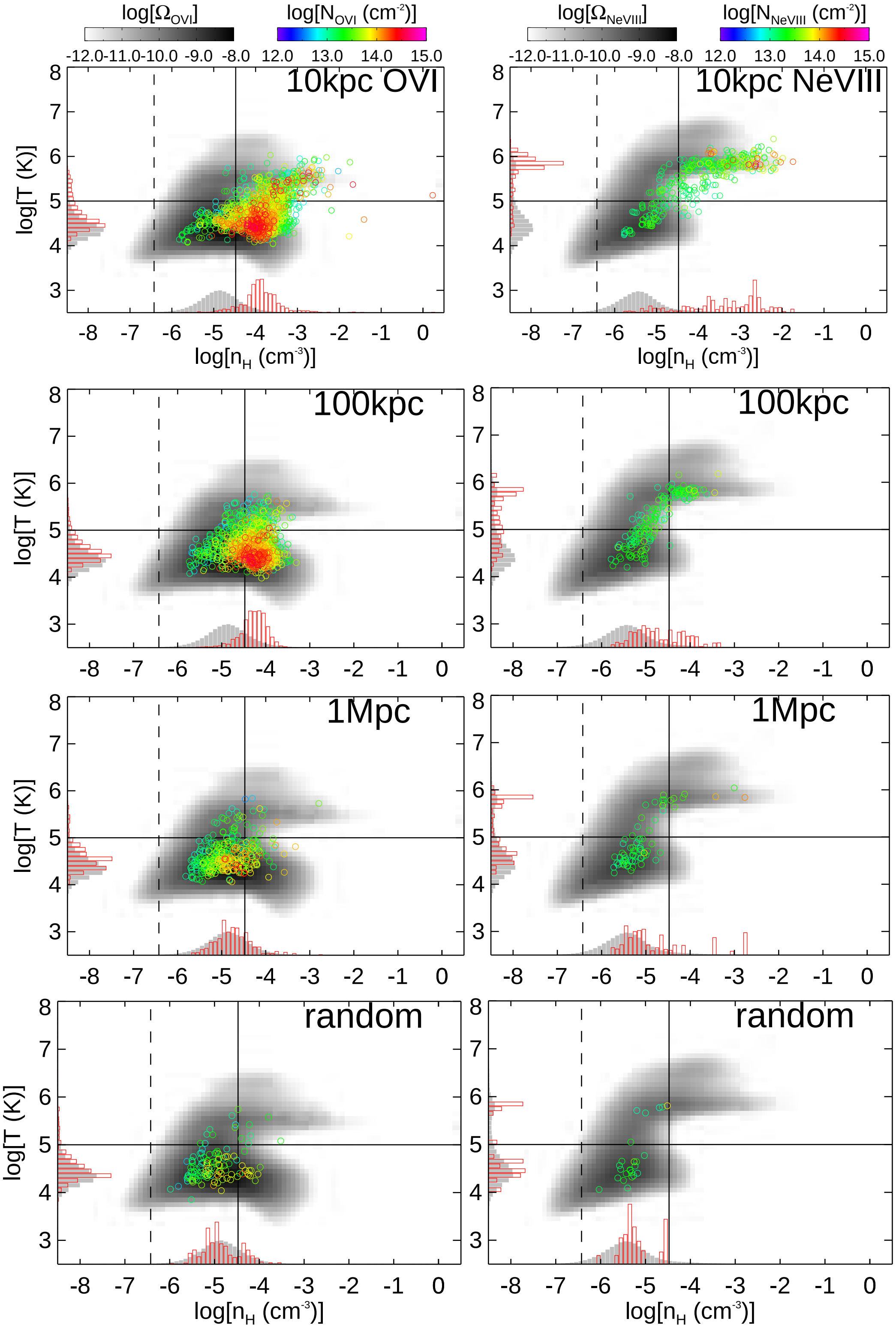

Figure 5. Analogous to Figure 3, phase space plots showing the location, in density and temperature space, of O VI (left) and Ne VIII (right) absorbers, for $M_h = 10^{12}\ M_\odot$, at the impact parameters indicated.

we subsample the absorbers from the random lines of sight chosen to cover an equivalent redshift pathlength.

The first clear trend from these figures is that the number of systems goes down with increasing impact parameter. The rate at which the number drops shows some differences among the various ions; we will explore this further in §6. The straightforward explanation for this is that both the metallicity and the gas density drop as one moves away from the galaxy, which translates into less metal absorption. Nonetheless, it is clear that even at 1 Mpc, there are more systems than in the random LOS (see §6).

Examining the plots more closely, one sees that for some ions there is a distinct shift in the overdensities probed by that ion as one moves out in impact parameter. This is most clear for the higher ionisation potential lines of O VI and Ne VIII, where the peak of the red histograms moves to lower overdensities at higher impact parameter, but it is also true for all other ions except Mg II. We remind the reader that the grey histograms are the same in every panel for each species because they correspond to the cosmic mass density of that ion, and thus we can interpret the red histograms as tracing a subset of the cosmic mass density.

To illustrate some of the information contained within these plots and histograms, consider C IV. At impact parameters of 10 kpc, C IV traces an average $n_{\rm H} \sim 10^{-3}$ cm^{-3} (red histogram), but the cosmic mass-averaged C IV density is $n_{\rm H} \sim 10^{-4}$ cm^{-3} (grey histogram). In fact, there is very little cosmic C IV at $n_{\rm H} > 10^{-3}$ cm^{-3}. However, 10 kpc from a galaxy inside a 10^{12} M$_\odot$ halo corresponds to a rare location in the Universe where there are high levels of metal enrichment and high densities, and hence C IV traces these metals. At impact parameters of 100 kpc, the red histogram for C IV peaks at 10^{-4} cm^{-3}, similar to the cosmic averaged peak in the grey histogram. However, the distribution of densities is narrower, indicating that absorbers at this impact parameter do not account for the full range of densities giving rise to all the C IV absorption. At impact parameters of 1 Mpc, C IV traces overdensities similar to the cosmic average. Finally, the random LOS C IV should theoretically trace the cosmic distribution of C IV and the red and grey histograms should overlap. However, as discussed in Oppenheimer et al. (2012), the absorber histogram is biased towards lower densities. The random LOS sample covering $\delta z = 2.5$ does not adequately sample densities with $n_{\rm H} > 10^{-4}$ cm^{-3} because this pathlength is not long enough to probe these rare high density regions. This illustrates a central tenet of this paper, namely that close-in targeted LOS probe regions of density that are not well-sampled via randomly chosen quasar absorption sight lines.

We can similarly examine other metal ions. Random LOS showing absorption from Mg II usually probe gas within roughly 10 kpc of galaxies. As a result, random LOS with Mg II absorption have the same overdensity as the 10 kpc gas. Meanwhile, Mg II absorption from further away generally probes lower density gas. For mid-ions, the random LOS have significant absorption farther away, and hence 10 kpc LOS pick out especially dense gas, but there is little distinction between 100 kpc, 1 Mpc, and random. For high ions, these arise in more diffuse gas so that the random LOS can probe quite low overdensities, and hence the LOS at 10 and 100 kpc pick out particularly denser gas.

Finally, for comparison, we examine neutral hydrogen. H I most closely resembles the general behaviours of Mg II, in that the cosmic density of H I is heavily weighted toward $n_{\rm H} > 10^{-2}$ cm^{-3} and most cosmic H I arises at small impact parameters going through ISM gas. There are, of course, a few key differences between the well-understood behaviour of H I and a metal-line species like Mg II. Most cosmic H I is in damped Lyα systems (DLAs), gas that is either within or near the galactic ISM (Wolfe et al. 2005), as indicated by the steadily rising grey histograms for H I. The Lyα forest tracing diffuse gas, i.e. column densities $N_{\rm H\,I} \sim 10^{13} - 10^{15}$ cm^{-2}, corresponds to an insignificant fraction of the total cosmic H I, unlike the high ionisation potential metal lines where most of the cosmic absorption arises from IGM and CGM densities. Also, H I can trace a relatively large range of phase space because: (i) hydrogen is present at all densities, (ii) Lyα has a high oscillator strength, and (iii) its presence does not rely on metal enrichment. A comparison of the red absorber histograms to the grey cosmic density histograms makes little sense for H I since all absorbers $> 10^{16}$ cm^{-2} have been reduced in our analysis to 10^{16} cm^{-2}, which hides most of the Lyα absorption from damped Lyα and Lyman-limit systems. However, the red histograms show a significant downward shift in overdensity going from impact parameter of 10 kpc out to 1 Mpc, reflecting the very different densities probed at these three impact parameters.

3.3 Physical Conditions vs. Ionisation Potential

Overall, the phase space plots illustrate a key general trend: the higher the ionisation potential of the metal species, the lower the overdensity that it traces on average, *and hence the further away from galaxies it arises.* We will argue that this is the case in our simulation because these metal species that we explore are primarily photo-ionised, except for high ionisation potential lines in massive halos.

To quantify these trends, Figure 6 plots the column density-weighted median overdensity (upper panel) – i.e., the overdensity above which 50% of the absorption occurs – of absorption systems of various ions, as a function of their ionisation potential for going from that ion into the next higher ionisation state. To compute the column-density weighted median value, we take, for each ion, all the systems for all the lines of sight and bin them according to their corresponding overdensity (or temperature), as in the red histograms from figures 3, 4 and 5. We then sum the column densities of all the systems in a given bin. We plot the overdensity (or temperature) corresponding to where half of the total column density (for all the bins) is above/below that value.

We also plot the column density-weighted median temperature (lower panel), i.e. the temperature above which 50% of the absorption occurs. Points are plotted for the well-defined median for a sample of 250 galaxies. To illustrate the range, we show vertical range bars (not error bars) that span the 16% to 84% enclosing values for the 100 kpc bin, as an example. This is the range of the overdensity (or temperature) above which 16% of the absorption occurs to the overdensity (or temperature) above which 84% of the absorption occurs. The different colour points represent the three different impact parameters, with black points showing the global values from the random LOS for comparison. These plots are for galaxies in halos with $M_{\rm halo} \approx 10^{12} M_\odot$.

We plot here the full range of column densities shown in Figures 3-5, but these findings do not depend significantly on the column density range probed.

Figure 6 (top panel) shows that the median density of metal absorption decreases steadily with ionisation potential, but that the rate of the decrease depends on impact parameter. Far from galaxies, the decrease is roughly two orders of magnitude from Mg II to Ne VIII. This reflects the predominantly photo-ionised nature of our absorption lines arising in diffuse gas far from galaxies, as elements require lower densities to achieve higher ionisation levels. The mean overdensity at 1 Mpc is essentially indistinguishable from that of the random LOS. At 10 kpc there is nearly as large a decrease in the median overdensity as a function of ionisation parameter as at 1 Mpc, but in each case the median overdensity is around two orders of magnitude larger at 10 kpc than at 1 Mpc. Impact parameters of 100 kpc are an interesting counterpoint, showing less than an order of magnitude difference in the mean overdensity from Mg II to Ne VIII. As we will discuss, this arises because in $10^{12}M_{\odot}$ halos the high ionisation potential lines start to have an additional contribution from collisionally ionised gas that occurs in the denser regions closer to galaxies.

The horizontal dotted line approximately delineates the overdensity boundary of virialised halos using Equation 1 from Davé et al. (2010). At 10 kpc, unsurprisingly, all the absorption in all the ions arises in gas that is within halos. At larger impact parameters and for the random LOS, the median overdensity depends strongly on the ionisation state, with ions having ionisation potentials lower than C IV generally arising in halo gas for $10^{12}M_{\odot}$ halos, while higher ionisation potential absorption often arises in gas with overdensities lower than that corresponding to galaxy halos. Unfortunately, this absorption is usually weak and photo-ionised (Oppenheimer et al. 2012), and hence generally still does not trace the so-called missing baryons in the WHIM.

Turning to the temperatures, Figure 6 shows that the median temperature of metal absorption rises steadily with ionisation potential. It also shows that, with the exception of Ne VIII, there is essentially no dependence of metal absorption gas temperature on the impact parameter. This reflects the fact that the majority of metal ions all arise in $\sim 10^{4-4.5}$ K gas, i.e. photo-ionised gas temperatures, regardless of the impact parameter. Note that the virial temperature in this halo mass range is about a million degrees, the upper boundary of the plot.

For Ne VIII at large impact parameters, the median temperature is around 30,000 K, still considerably lower than its collisional ionisation peak temperature of 10^6 K, and owes to photo-ionised gas. This begins to change as one approaches galaxies. At 100 kpc, about half of the absorption comes from gas above 200,000 K, and at 10 kpc most of the Ne VIII is hot, with half the absorption coming from gas above 500,000 K that is collisionally ionised. Since (as is evident from the phase space plots) these Ne VIII absorbers are also stronger, we obtain a result matching that of Oppenheimer et al. (2012) that strong Ne VIII absorbers are more often collisionally ionised. By using our targeted LOS, we show here that this mostly arises from Ne VIII within 100 kpc of galaxies, at least in these $10^{12}M_{\odot}$ halos. As hypothesised in Oppenheimer et al. (2012), these strong lines are probably the only ones that have been studied carefully with COS to date (e.g., Tripp et al. 2011), but larger and deeper samples should uncover a population of photo-ionised Ne VIII arising in more diffuse gas.

This hot gas close to galaxies is also evident in the H I, where at 100 kpc half the H I absorption traces gas that is above 50,000 K, and much of this gas is above the halo virial density. Even at 1 Mpc there is some hot H I, as the median temperature is still fairly high at 40,000 K, even though the median overdensity is quite low. As one can see from Figure 3, there are a number of absorbers than can arise from both hot halo gas and truly diffuse WHIM gas. Hence, in principle, broad H I absorbers could trace truly diffuse WHIM gas (i.e. the missing baryons), but one has to be careful not to count hot halo gas, which may be detectable by other means.

Our simulations predict that even high ions are mostly photo-ionised at all radii. This is at odds with recent work by Stinson et al. (2012), whose simulations find that O VI is predominantly collisionally ionised in their individual galaxy simulations. Their model has the advantage of having higher resolution than ours, but our models have the advantage that our feedback prescription has been carefully constrained to match a broad range of observations, including IGM enrichment. The main difference is likely that their feedback model relies on super-heating gas within the ISM that drives hot gaseous outflows, whereas our model follows scalings expected for momentum-driven winds in which the gas is pushed out via radiation pressure, and therefore is not super-heated. Our outflows do heat once they interact with surrounding gas, but since they are typically quite enriched, the metal-enhanced cooling rates are rapid. Simply put, their feedback model adds hot gas to the halo by construction, while ours adds cooler gas by construction; it is not immediately evident which is closer to correct, and likely depends on the details of how winds are actually launched which is currently not well understood. Stinson et al. (2012) did not show the O VI temperature as a function of radius, area-weighted as would be appropriate for an absorption line survey, so it is difficult to compare our results directly. But these differences highlight that modeling the CGM is not a fully solved problem. Examining such detailed statistics as line ratios and alignment statistics between O VI and H I (and low metal ions, e.g. Si III) provides a way to characterize the temperature of the O VI gas and discriminate between such scenarios. We note that at least in the random lines of sight examined in Oppenheimer & Davé (2009), the observed alignment statistics between O VI and H I were better reproduced in a momentum-driven wind scalings model as opposed to our constant wind model that yielded more collisionally-ionised O VI. We are conducting such comparisons now against COS-Halos data.

In summary, different metal ions probe different physical conditions around galaxies, with lower ionisation potential lines probing denser gas. Mg II absorbers probe very high density gas in and around the ISM of galaxies, while high ionisation potential lines probe diffuse gas in the outskirts of halos and beyond the virial radius. The absorbing gas temperatures generally reflect the photo-ionised nature of metal absorption even down to small impact parameters in our models, with the notable exception of Ne VIII lines that can arise in hot gas near galaxies. In the next section we will show that O VI in larger halos where a hot CGM is present is

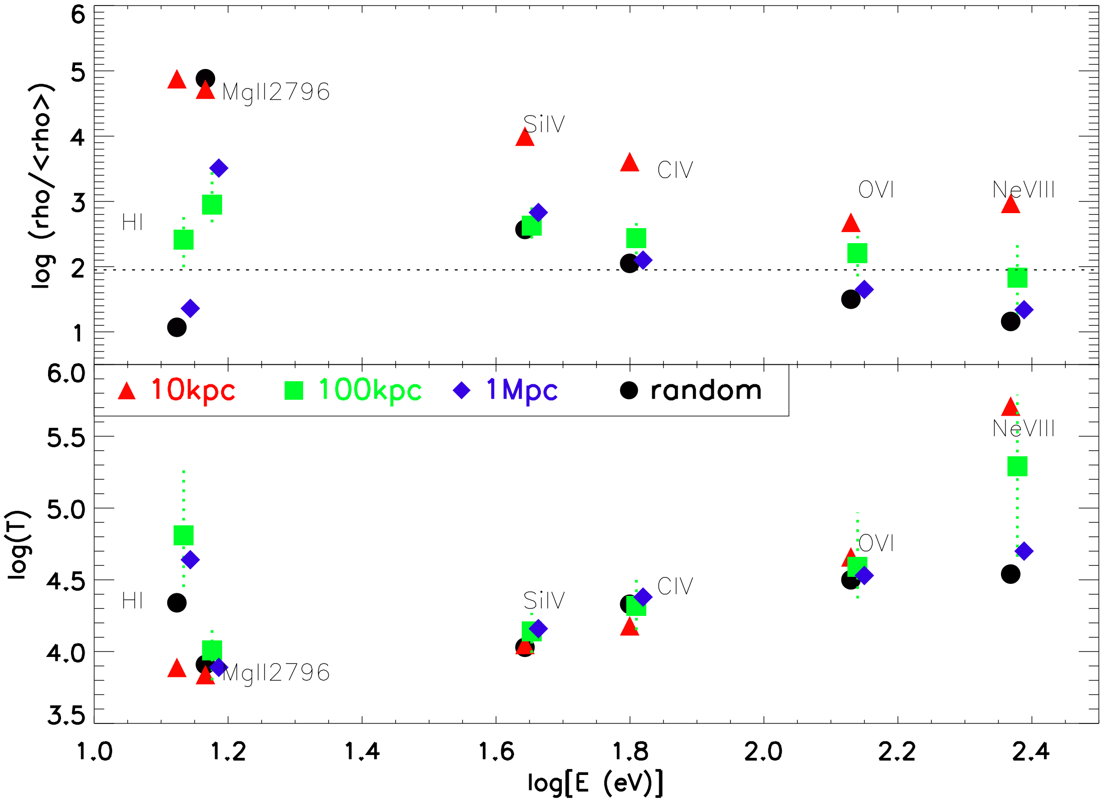

Figure 6. *Top panel:* Median column density-weighted overdensity as a function of ionisation energy for the six ions we consider. Four points for each ion are plotted, corresponding to three different b values (all for mass bin 10^{12}) and random LOS. 100 kpc (green squares) and random (black circles) are plotted at the energy in eV at which the labeled ion is ionised to the next higher level; 10 kpc (red triangles) and 1 Mpc (blue diamonds) are shifted for visibility. Points are plotted at the well-defined median; vertical range (not error) bars (shown only on the 100 kpc case for clarity) span the 16% to 84% enclosing values. The dotted horizontal line represents the virial overdensity at $z = 0.25$. *Bottom panel:* Similar to the top panel, but for column density-weighted temperatures.

also mostly collisionally ionised. These results demonstrate that spanning a range of ions with low to high ionisation potentials can in principle probe a wide range of physical conditions in the CGM, but that when a range of ions are seen in a single system, it is probably unwise to assume that they all arise from the same gas (for the purposes, e.g., of CLOUDY modeling). Throughout the rest of this paper, we will discuss our results in terms of low (Mg II), mid (Si IV and C IV), and high ionisation (O VI and Ne VIII) lines, since this provides an underlying physical context for understanding the behaviour of these various metal absorbers.

3.4 Physical Conditions vs. Halo Mass

The previous section focused entirely on $10^{12} M_\odot$ halos, as representative of a typical L^* galaxy halo. However, the increasing collisional ionisation contribution to the higher ionisation potential species might suggest that there could be some halo mass dependence since, as is evident in Figure 2 and has been shown by e.g. Kereš et al. (2005), large halos have substantially more hot gas.

To investigate any trends with halo mass in Figure 7, we plot in the top panels the column density-weighted median overdensity and temperature as in Figure 6, here as a function of halo mass, focusing on H I (left panel), O VI (middle panel), and Ne VIII (right panel). As in Figure 6, we plot the full range of column densities shown in Figures 3-5, but these findings do not depend much on column density range probed. We show three different impact parameters, slightly offset horizontally for ease of visibility, and here we show the $16-84\%$ range for all cases. The points for galaxies in halos of $10^{12} M_\odot$ are identical to those shown in Figure 6. We do not show the random LOS here; the values are similar to the 1 Mpc case. We also do not show the other ions, because in those cases there are no discernible trends with halo mass.

At 10 kpc, for H I, the absorption arises from low temperature gas for all mass bins. While Figure 2 shows halos of mass $10^{13} M_\odot$ have high median temperatures, Figure 7 shows the HI absorption mostly comes from low temperature gas present in these halos. For absorption around galaxies in halos of $10^{11} M_\odot$, most of the O VI and Ne VIII absorption owes to gas with overdensities lower than that found in galaxy halos, since the densities are below the dotted virial overdensity line. The exception is O VI at 10 kpc, where about half the absorption comes from the outskirts of halos. Both high ionisation potential lines have a median temperature within the photo-ionised regime at all impact parameters (although for Ne VIII there is a tail to higher temperatures for impact parameters of 1 Mpc). Hence O VI and Ne VIII absorption around galaxies with halo masses of $10^{11} M_\odot$ actually traces photo-ionised, diffuse IGM gas. This occurs because there is so little hot gas in these small halos (Kereš et al. 2005) that there is little opportunity for these ions to trace collisionally ionised gas.

For galaxies in $10^{12} M_\odot$ halos, the temperatures are still mostly representative of photo-ionised gas for O VI, but Ne VIII begins to trace somewhat hotter gas, already indicating a contribution from collisionally ionised gas at smaller impact parameters. At impact parameters of 10 kpc, this gas is within galaxy halos for both ions, and even at 100 kpc almost all the O VI absorption and about half the Ne VIII absorption owes to gas with an overdensity consistent with being within galaxy halos. At impact parameters of 1 Mpc, the gas giving rise to this high ionisation potential absorption still mostly arises from gas outside of galaxy halos.

Finally, for galaxies in $10^{13} M_\odot$ halos, we see a strong dependence of physical conditions on impact parameter, with the density and temperature both being substantially higher at smaller impact parameters. At impact parameters of 10 kpc and 100 kpc for both ions, all the absorption owes to gas within galaxy halos that is at temperatures indicative of collisional ionisation. This reflects the substantial presence of hot, virial-temperature gas within these halos. At impact parameters of 1 Mpc, however, the absorption still mostly arises from photo-ionised, diffuse IGM gas.

In summary, the high ionisation potential lines tend to trace collisionally ionised hot gas when it is present. But this gas is generally only present abundantly well inside of halos, at impact parameters of less than 100 kpc, and only in massive halos where a hot gaseous atmosphere can form. In those cases, these (and other high ion) lines may trace hot gas in halos that are not easily probed by X-ray emission (or absorption lines), offering a unique opportunity to study these baryons.

4 ABSORPTION AROUND GALAXIES IN REDSHIFT SPACE

The distance of an absorber from a galaxy can be observationally characterised by two parameters: the line-of-sight velocity difference Δv and the impact parameter b. In this section we discuss the former, i.e. how absorption properties vary with the velocity distance from the central galaxy. We seek to answer questions like the following: Does the absorption drop off with Δv at different rates for different ions? Can we identify a characteristic LOS velocity distance over which the galaxy provides a clear excess of absorption? How do these tendencies reflect the physical conditions of the absorbing gas?

Figure 8 shows the column density (N) versus velocity separation (Δv) from the central galaxy for each of our six ions, with the species ordered by increasing ionisation potential going down the columns. The lines show the median column densities for all lines of sight at the three different impact parameters: 10 kpc (red), 100 kpc (green), 1 Mpc (blue), for the three different halo masses: $10^{11} M_\odot$ (dotted), $10^{12} M_\odot$ (solid), and $10^{13} M_\odot$ (dashed). We use 100 $\mathrm{km\,s^{-1}}$ bins and plot at the bin's midpoint. For example, $\Delta v = 150$ $\mathrm{km\,s^{-1}}$ plots the total column density between $\pm(100-200)$ $\mathrm{km\,s^{-1}}$. Note that the y axis has a rather large range; most of this range is not accessible observationally, but we include it to accentuate the trends.

The median column density decreases with increasing Δv for all the ions, following the trend highlighted before that the absorption tends to be higher near galaxies. Except at high halo masses, there are drops in these curves before ± 300 $\mathrm{km\,s^{-1}}$. Conservatively, we may say that the vast majority of absorption generally occurs within ± 300 $\mathrm{km\,s^{-1}}$ of the central galaxy's velocity, although in many cases the majority occurs within a smaller velocity interval. We choose to define the velocity window associated with the galaxy as 300 $\mathrm{km\,s^{-1}}$ to account for as much absorption in the higher mass halos as possible while not going far beyond the drops in the lower mass halos. We note that ± 300 $\mathrm{km\,s^{-1}}$ is roughly consistent with recent observational work by Prochaska et al. (2011). Quantitatively, we can consider the total amount of absorption within ± 300 $\mathrm{km\,s^{-1}}$ relative to total absorption within ± 600 $\mathrm{km\,s^{-1}}$. Looking at all three impact parameters, O VI has at least 96% of its column density within this velocity limit for $M_{\rm halo} = 10^{11}$ $\mathrm{M_\odot}$, 97% for $M_{\rm halo} = 10^{12}$ $\mathrm{M_\odot}$, and 88% for $M_{\rm halo} = 10^{13}$ $\mathrm{M_\odot}$. The absorption of lower ionisation potential metal species falls off even faster with increasing velocity difference. This indicates that in general one has to look only within the central 600 $\mathrm{km\,s^{-1}}$ window around a galaxy to find most of the absorption associated with it.

Absorption around galaxies in our most massive halo bin, $10^{13} M_\odot$, shows a shallower decrease with increasing Δv, reflecting these halos' larger virial velocities and hence larger peculiar motions of gas and satellites. While the ± 300 $\mathrm{km\,s^{-1}}$ cut misses some absorption in the large halos at small b, LOS passing so close to such massive galaxies are rare. Henceforth, we only consider absorption within ± 300 $\mathrm{km\,s^{-1}}$ of galaxies for our targeted LOS in the subsequent figures.

Now we examine the differences between the various metal ions. The low ionisation potential ions decrease in absorption more rapidly with increasing impact parameter than high ionisation potential ions. The column densities of Si IV and C IV at fixed Δv drop rapidly from 10 kpc to 100 kpc, and at 1 Mpc they are not even visible in this plot. In contrast, the high ionisation potential ions, O VI and Ne VIII, show essentially no decrease in absorption at fixed Δv when the impact parameter increases from 10 kpc to 100 kpc, and the drop from 100 kpc to 1 Mpc is more modest than for low ionisation absorbers. The decrease in column density is also more dramatic with increasing Δv for the low ionisation potential ions. This occurs because high ionisation potential lines arise in more extended gas distributions at lower overdensities, which trace the general large-scale structure in which galaxies live, while the low ionisation potential ions are more confined to the high-density gas found closer to galaxies (as seen in Figure 2).

In this plot, H I behaves much like a high ionisation potential line – note the similarity in the shapes of the curves between H I and O VI, although there is a large difference in the magnitude of the column densities. This reflects the fact that H I can arise in a wide range of physical conditions, and even at small impact parameters there is a substantial contribution to the column density from gas along the LOS out to large Δv's (Kollmeier et al. 2003; Kollmeier et al. 2006).

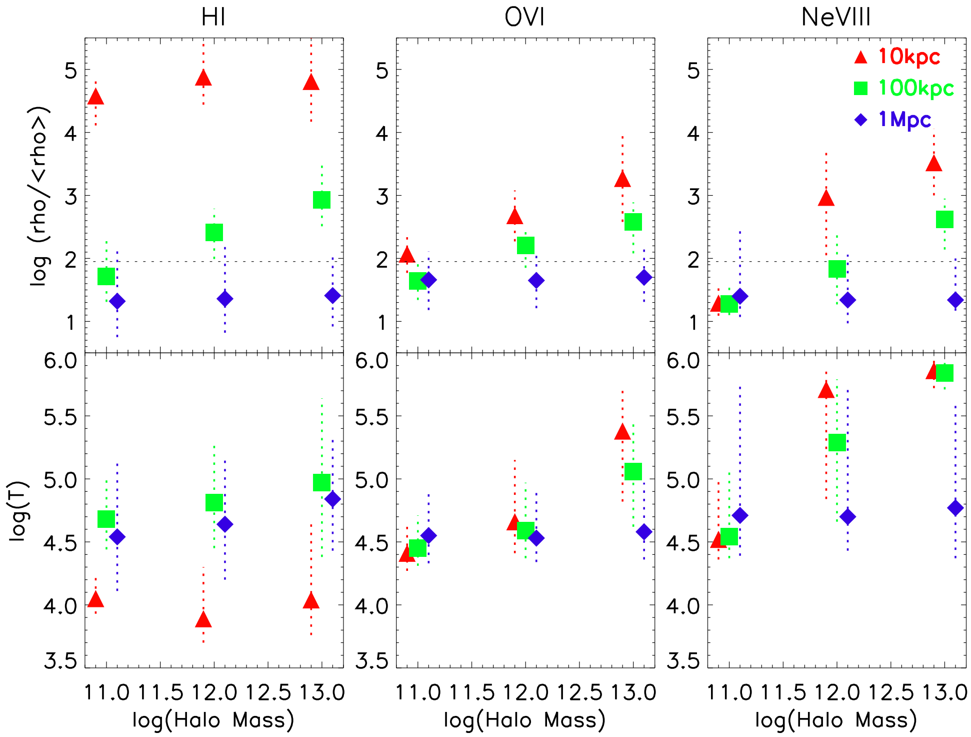

Figure 7. Median column density-weighted overdensity and temperature vs. halo mass for H I (left panels), O VI (middle panels), and Ne VIII (right panels). For all panels, the different colours correspond to the three different impact parameters: 10 kpc (red triangle), 100 kpc (green square), and 1 Mpc (blue diamond) (offset for clarity). The range bars span the 16% to 84% enclosing values, and the dotted horizontal line represents the virial overdensity.

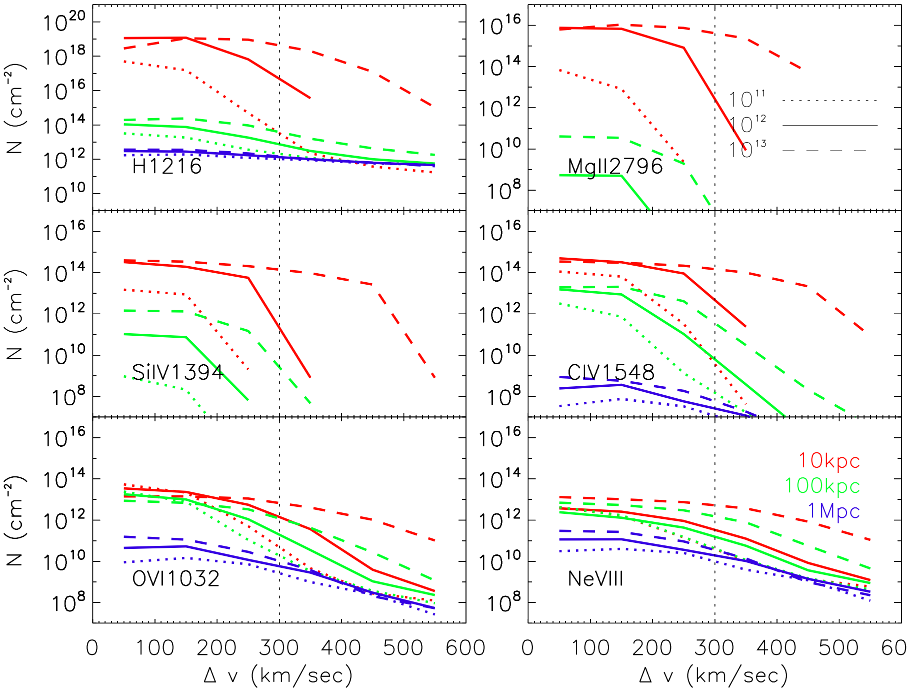

Figure 8. Median column density (N) vs. velocity separation (Δv) from the central galaxy Δv for $M_h = 10^{11,12,13} M_\odot$ (dotted, solid, and dashed lines, respectively). We show results at three impact parameters: 10 kpc (red), 100 kpc (green), and 1 Mpc (blue). Vertical dotted lines mark 300 km s^{-1}.

At 1 Mpc, H I absorption does not depend much on the central halo mass. H I is observed almost everywhere that metal ions are seen, and in almost every case has a column density greater than any metal ion.

Finally, we examine the trends with halo mass. Nominally, the larger peculiar velocities within larger halos should result in greater Δv's; each factor of 10 in halo mass should correspond to a factor of $10^{1/3} \approx 2.2$ in Δv. In practise, one would expect Δv differences that are somewhat lower than this because one integrates the column density through the entire halo. Low ionisation potential ions like Mg II are close to this expectation, with the differences between the curves being roughly a factor of 1.7 in Δv. This indicates that Mg II basically arises only when the LOS intercepts a galaxy, and at large Δv the satellite galaxies giving rise to the absorption are tracing the underlying halo potential. The mid ionisation potential ions Si IV and C IV are similar to Mg II, indicating that the denser gas giving rise to these ions also traces the underlying potential. Moving towards higher ionisation potential lines, we see somewhat smaller differences as a function of halo mass, as absorption in these ions starts to pick up gas that is outside the virial radius and hence not dominated by the halo potential. It is important to note once again that all the massive galaxies in the vzw simulation have star formation rates well above comparable-mass galaxies in the real Universe, owing to a lack of a quenching mechanism in our simulations (e.g. Gabor & Davé 2012). Therefore, the absorption trends at higher mass may not be reflective of the real Universe, where the observed O VI declines in strength in more massive halos (Tumlinson et al. 2011). Nonetheless, to first order for all ions, close to galaxies it is the dynamics of the host halo that establishes the Δv distribution of the absorption.

In summary, all ions have the vast majority of their absorption arising within a redshift-space distance of (conservatively) $\Delta v\pm$ 300 km s^{-1} around galaxies for all but the most massive halos. Low ionisation species show a sharp drop with Δv, while high ionisation species show a more gradual drop. More massive halos show a broader absorption distribution in Δv reflecting their larger potential wells. For low ionisation lines, absorption drops very rapidly with impact parameter, while for high ionisation lines, the drop with impact parameter is much slower. These trends broadly reflect the overall morphology of absorption relative to galaxies, in the sense that lower ionisation lines are more confined to dense gas closer to galaxies.

5 ABSORPTION AROUND GALAXIES VERSUS IMPACT PARAMETER

We now turn to examining the extent of absorption around galaxies in physical space, as quantified by the impact parameter *b*. From the previous section, we know that much of the absorption occurs within approximately ±300 km/s of a galaxy (the mild exception being for low ionisation potential lines in massive halos). Hence, we will examine how absorption within this Δv range varies with impact parameter, as a function of both ionisation level and halo mass.

In Figure 9 we plot the summed column density per unit redshift along all lines of sight with a given impact parameter, with the impact parameters ranging from $10-1000$ kpc. We show results from our vzw simulation for galaxies in halos with masses of $10^{11} M_\odot$ (dotted lines), $10^{12} M_\odot$ (solid), and $10^{13} M_\odot$ (dashed). We show error bars owing to cosmic variance (since statistical errors are small). To calculate those, we divide our simulation volume into sixteen sections of equal volume and compute the dN/dz values for lines of sight within each section, and compute the dispersion over the sixteen sections. We ignore the (rare) sections that have no absorption when calculating the dispersion.

Here, we have chosen to plot a summed column density, instead of a median one. This is because we are interested in predicting the total absorption along the line of sight as one moves out in impact parameter. The median value can be highly dependent on the resolution and noise level of the spectra, since better quality spectra will result in many more weak lines. In contrast, the summed absorption is a more robust quantity. However, it does have the disadvantage that it can be biased by a single, very large absorber. To mitigate this, we apply here the same column density caps as described in §3.2. Lines above 10^{16} cm^{-2} for H I and 10^{15} cm^{-2} for metal lines are reset to 10^{16} cm^{-2}and 10^{15} cm^{-2}, respectively. While this particular statistic has yet to be determined observationally as a function of impact parameter, this could certainly be done, and would provide a robust quantitative estimate of the total amount of absorption as one moves away from galaxies.

The trends seen here in physical space are qualitatively similar to those seen in redshift space in the previous section. All the ions show enhanced absorption near galaxies; even at 1 Mpc the dN_{ion}/dz for targeted LOS is noticeably higher than that for random LOS, shown as the diamond at 1 Mpc in each plot. For low and mid ionisation potential ions, the decline is very steep with increasing radius, and beyond a few hundred kpc, dN_{ion}/dz is almost independent of impact parameter. For Mg II, the dN/dz value has dropped by two orders of magnitude by 100 kpc. For mid ions, the sharp drops in dN/dz happen at slightly further impact parameters, roughly 200-300 kpc. For high ionisation potential ions, the decline is not as steep with impact parameter, but there is still a clear enhancement within roughy 300 kpc; about a factor of two for O VI and about a factor of four for Ne VIII.

There are also trends with halo mass, although they are not strong as in Figure 8. The general trend is that there is somewhat more absorption at higher halo masses, at most impact parameters. To first order, this reflects the increased gas density both in and around larger halos. There are some interesting exceptions; for instance, O VI shows less absorption within 200 kpc for galaxies in massive halos. This may reflect temperatures deep within group-sized halos that exceed the collisional ionisation temperature of O VI (Davé, Oppenheimer, & Sivanandam 2008) combined with densities that exceed the photo-ionisational densities of O VI (Oppenheimer & Davé 2009). When one reaches 1 Mpc impact parameters, the dN_{ion}/dz values for H I and the high ionisation potential ions for the various halo masses all have essentially converged.

We have argued above somewhat indirectly that most metal absorption arises from gas within roughly 300 kpc of galaxies (depending on the ion), but in simulations we can test this hypothesis directly. To do so, we tag gas particles in our simulations that lie within a chosen ra-

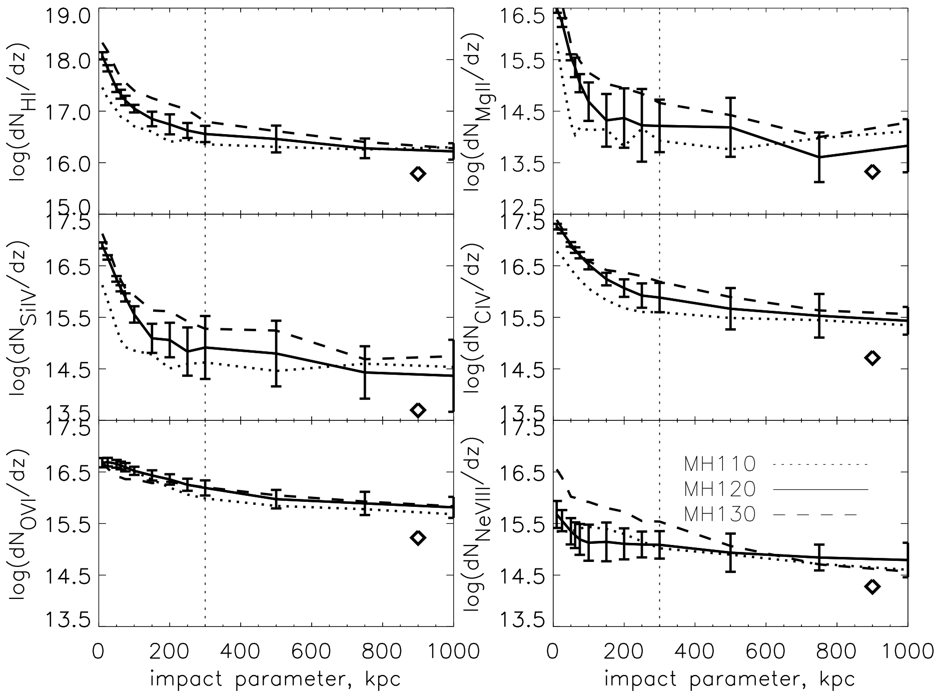

Figure 9. The total column density (not number density) per unit redshift versus impact parameter around galaxies in halos of $10^{11} M_{\odot}$ (dotted), $10^{12} M_{\odot}$ (solid) and $10^{13} M_{\odot}$ (dashed). For halos, dN/dz is the summed column density for the given ion along all lines of sight at the given impact parameter over the velocity range ± 300 km s^{-1}, divided by $\Delta z = (\text{Number of halos in sample}) \times (600 \text{ km s}^{-1})/(1+z)$. The black symbols indicate dN/dz for random lines of sight. Note that the vertical range for each ion varies, although it always spans 4 dex. The vertical dotted line corresponds to 300 kpc. Error bars show the cosmic variance across sixteen simulation sections of equal volume.

dius r from any resolved SKID-identified galaxy ($M_* \geqslant 10^{9.1}$ $M_{\odot}$), and then regenerate our LOS with contributions only from those tagged particles. We exclude galaxies below this mass limit as they are not well resolved in our simulations (Finlator et al. 2006). Figure 10 shows the resulting summed dN_{ion}/dz values as a function of impact parameter, analogous to Figure 9, with the different lines showing the contribution from particles within $r < 30$ kpc (blue dotted), $r < 100$ kpc (green dashed), and $r < 300$ kpc (red dot-dashed) from galaxies. We show here results for the $10^{12} M_{\odot}$ halo mass bin, but the results are not significantly different for other halo masses. For comparison, the solid black line includes absorption from all gas, reproduced from Figure 9.

Explaining further, in this Figure we use the same galaxies as in Figure 9, with the same LOS at the same impact parameters. But we no longer consider absorption from every SPH particle that intersects the targeted LOS. We now consider absorption from the SPH particles along the line of sight *only* if they are within a given physical radius from *any* galaxy in our simulation volume, *not just the targeted one.* The reader will note that, for example, the red 300 kpc line extends past 300 kpc. This is due to clustering. A targeted line of sight can find absorbers at, for example, 750 kpc because those absorbers are from particles within 300 kpc of another galaxy, as opposed to the targeted one.

Table 2. For each ion, we give the percentage of absorption from particles within 300 kpc of any galaxy in our simulations, at each impact parameter listed. Values in this table are derived from the difference between the red dash-dotted and black solid lines in Figure 10 at impact parameters of 10, 100, and 300 kpc.

	10 kpc	100 kpc	300 kpc
H I	94%	81%	41%
Mg II	97%	97%	80%
Si IV	96%	97%	80%
C IV	96%	92%	66%
O VI	79%	74%	35%
Ne VIII	67%	32%	14%

For the low and mid metal ions, particles within 300 kpc are responsible for the great majority of the absorption at all impact parameters, as given in Table 2. For low ionisation species, particles within even smaller radii are responsible for the majority of absorption. For Mg II, most of the absorption owes to particles within only 100 kpc, and typically around half of the Mg II absorption owes to gas within only 30 kpc of galaxies. For mid ions Si IV and C IV, essentially all the absorption comes from within 300 kpc of galaxies, with the majority of it from within 100 kpc, and only a small fraction within 30 kpc. For O VI and Ne VIII, how much absorption comes from particles within 300 kpc depends upon impact parameter, as shown in Table 2. For these high ions, very little of the absorption comes from particles within 100 kpc, and in fact a substantial fraction can come from particles further than 300 kpc from galaxies. The contributions to the 100 kpc curves at $b > 100$ kpc, for example, must come from

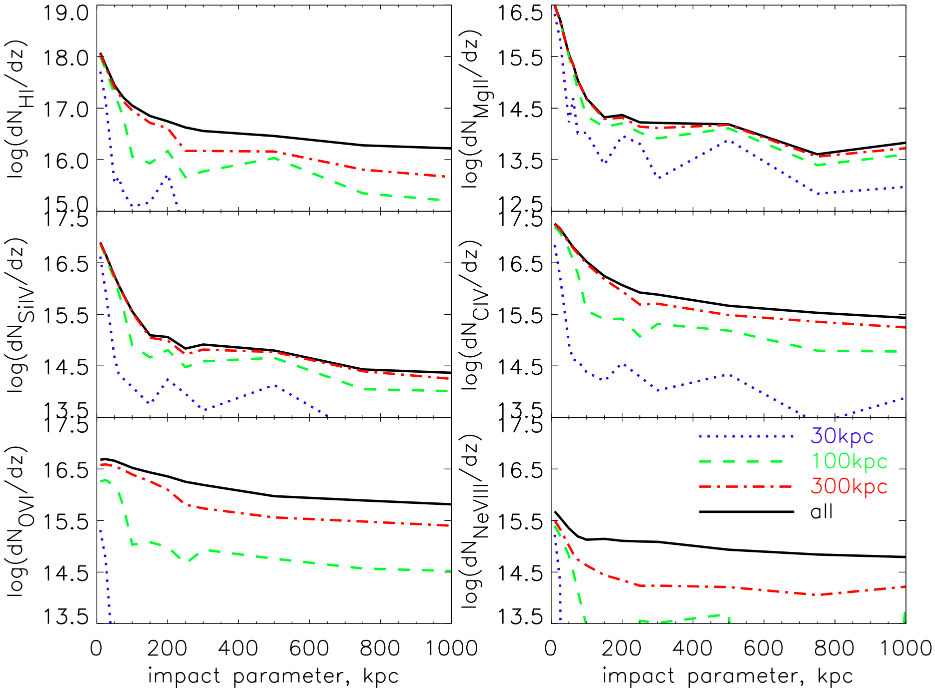

Figure 10. Total column density per unit redshift (dN/dz) for targeted LOS around $10^{12}M_\odot$ halos, for all gas particles (black solid line, identical to Figure 9), and for gas within the specified radius of a galaxy (coloured lines). Black line is labeled "all", indicating that we consider absorption from all SPH particles (i.e. the full simulation) intersecting the targeted LOS. Coloured lines indicate dN/dz where we only include absorption from SPH particles that are within a sphere of the indicated physical radius from *any* galaxy in our simulation (not just the targeted one). Dotted purple shows dN/dz for gas within 30 kpc (physical) of a galaxy, Dashed green line is for 100 kpc, and dash-dot red is for 300 kpc.

gas associated with other galaxies, either satellite systems or galaxies projected along the LOS with $|\Delta v| < 300$ km s^{-1}.

In summary, the extent of metal ions around galaxies – that is, the range containing the vast majority of metal absorption – is roughly 300 km s^{-1} in velocity space (although in some cases much less than that), and roughly 300 kpc in physical separation (except for O VI and Ne VIII at large impact parameter). Low ionisation potential metal ions are more confined around galaxies in both velocity and physical space. This is consistent with the visual impression of the column density images in Figure 2. We reiterate that metal ions are more likely to be found within 300 kpc or 300 km s^{-1} of *some* galaxy, not necessarily the target galaxy. In particular, the excess of low ions at large radii in Figures 9 and 10 arises from satellites and neighboring galaxies.

6 COLUMN DENSITY DISTRIBUTIONS

The column density distribution (CDD), i.e. the number of absorption systems per unit column density per unit redshift, represents the most basic counting statistic for characterising absorption line systems. Examining the CDDs as a function of impact parameter tells us how absorption drops off with distance as a function of column density, and thereby gives us a more detailed view of how absorption varies around galaxies compared to the aggregate statistics presented in the previous sections.

Figure 11 shows CDDs plotted as $N^2 \times f(N)$ where $f(N) \equiv d^2n/dNdz$ for all our ions, where N is the column density, n is the number of lines, and dz is the redshift-space path length, corresponding to ± 300 km s^{-1}. We plot this at three impact parameters of 10 kpc (red), 100 kpc (green), and 1 Mpc (blue), and for comparison we also plot the CDD for random LOS (black; similar to those in Oppenheimer et al. 2012). As before, we combine ions with separations $\Delta v < 100$ km s^{-1} into systems before measuring the CDD, and apply column density caps (see §3.2). In the top panel, we add colored circles indicating the center of the distribution, i.e., where 50% of the total column density is below that value and 50% above it. In the bottom panel we indicate these central values with triangles and squares for $10^{11}M_\odot$ and $10^{13}M_\odot$, respectively. The top panels show the results for galaxies in halos of $\approx 10^{12}M_\odot$. The bottom panels show analogous CDDs for galaxies in halos of $\approx 10^{11}M_\odot$ (dotted lines) and $\approx 10^{13}M_\odot$ (dashed) to assess the dependence on halo mass.

We multiply $f(N)$ by N^2 to obtain a quantity that reflects the (relative) amount of absorption per unit redshift at each column density in that ion: the value of $N^2 \times f(N)$ at $N = 10^{14}$ cm^{-2}, for example, represents the total column density per unit redshift contributed by lines in a $\Delta \ln N = 1$ interval centered at $N = 10^{14}$ cm^{-2}. Multiplying by N^2 also enhances the visibility of trends by mitigating the typically steep power-law dependence of $f(N)$. In previous work (Oppenheimer et al. 2012; Davé et al. 2010), we had plotted

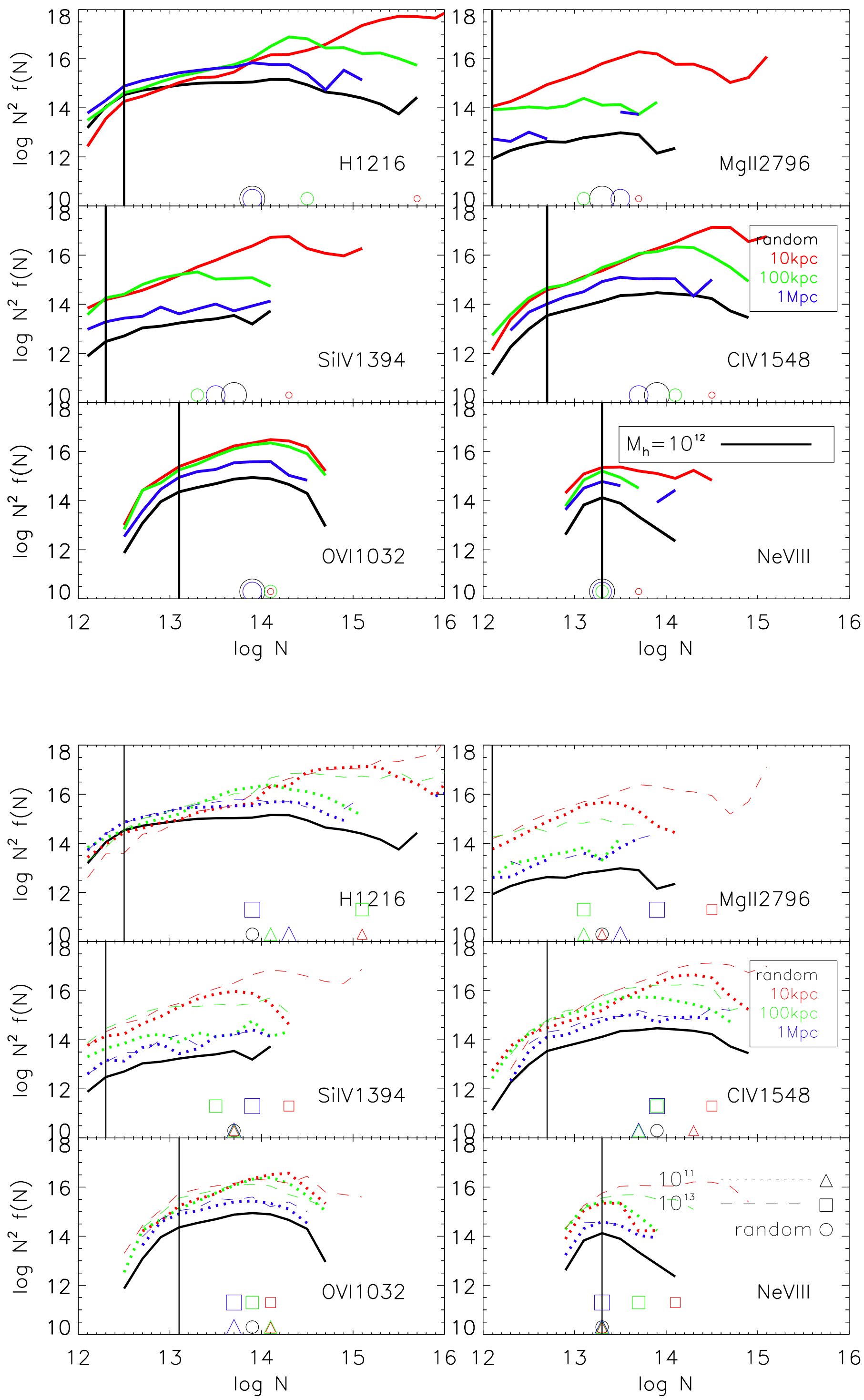

Figure 11. Top panel: Column density distributions (CDDs) for galaxies with $M_{halo} = 10^{12} M_\odot$. $f(N) \equiv d^2n/dNdz$. We multiply $f(N)$ by N^2 to show from where most of the absorption per unit log column density arises. The black line is the column density distribution for random LOS, red, green, and blue are for targeted LOS at 10 kpc, 100 kpc, and 1 Mpc, respectively. Circles (which increase in size with increasing b) mark the peak of the distribution, i.e., where 50% of the column density is below that value and 50% above it. Bottom: Same as the top panel for galaxies in halos of $10^{11} M_\odot$ (dotted line) and $10^{13} M_\odot$ (dashed line). Triangles and squares mark the peak of the distribution for $10^{11} M_\odot$ and $10^{13} M_\odot$ respectively, also increasing in size with increasing b, while circles mark peak for random distribution, as in top panel. Vertical lines show the completeness limit of the CDDs for S/N=30 per 6 km s^{-1} pixel.

$N \times f(N)$ just for visibility's sake. Here we add an additional power of N, because this means that the crest of the $N^2 \times f(N)$ curve represents the column density contributing the most absorption per logarithmic interval in that ion. These crests are typically shallow — indicating absorption that is spread over a fairly wide range of column densities — but they correspond well to the centers of the cumulative distributions marked by the circles.

We plot a vertical line that represents the 50% completeness limit for the CDD of absorbers identified in our artificial spectra with S/N=30. We determine this limit by comparing these CDDs to those derived from artificial spectra with S/N=100 (not shown) and by identifying the column density where the S/N=30 CDD begins to deviate by more than 50% from the CDD derived with S/N=100. We determine this limit using random LOS since this sample contains the largest total number of lines owing to its large path length. Since we employ the same S/N in all spectra, this completeness limit should also be applicable for the targeted LOS.

The first thing that one gleans from these figures is that for the metals, even at impact parameters of 1 Mpc there is clearly more absorption near galaxies than in the random LOS. This is true for every ion and for the full range of halo masses that we explore in this paper. For low ions that arise predominantly near galaxies, this reflects the large-scale auto correlation function of galaxies, which extends to many megaparsecs. For high ionisation potential ions, the absorption arises in less dense (diffuse and WHIM) gas that still correlates with galaxies living in large-scale structures.

We also see that the cosmic absorption in every metal ion peaks in the range of $N \approx 10^{13} - 10^{14.5}\mathrm{cm}^{-2}$. These peaks are generally above the completeness limit for all the ions except Ne VIII, where the lines are intrinsically weak. For the lower ionisation potential ions (Mg II, Si IV, C IV), this peak moves to larger columns as one goes to smaller impact parameters, while for the high ionisation potential ions the peak remains mostly independent of the impact parameter. In addition, for high ionisation potential ions (and for Mg II) one must probe to fairly low column densities to capture the bulk of the cosmic absorption, e.g., $N_{\rm OVI} \sim 10^{14}\mathrm{cm}^{-2}$ and $N_{\rm NeVIII} \lesssim 10^{13.5}\mathrm{cm}^{-2}$. Hence, while many O VI and Ne VIII absorption systems are now being detected in COS data (Tumlinson et al. 2011; Tripp et al. 2011), our models predict that higher S/N observations that probe to $N \sim 10^{13.5}\mathrm{cm}^{-2}$ are needed to capture the bulk of cosmic absorption in these ions.

Now let us examine H I, as this ion is relatively well understood in terms of its connection with galaxies and large-scale structure (e.g., Davé et al. 1999; Davé et al. 2010). H I shows a clear trend of having an increasing number of high column density absorption systems as one approaches a galaxy, i.e. as one goes to small impact parameters. In contrast, as one goes to smaller impact parameters the number of lower column density absorption systems does not change as significantly. In fact, below $N \sim 10^{14}\mathrm{cm}^{-2}$ the trend actually reverses with the number of systems increasing as one goes to larger impact parameters. This can be easily understood. The strong absorbers mostly arise in the dense gas around galaxies, while the weak absorbers arise more in the surrounding large-scale structure, even when the impact parameter is small. This is consistent with the strong correlation between H I column density and overdensity predicted in the models (e.g., Davé et al. 2001; Schaye 2001; Davé et al. 2010; Hui et al. 1997).

For the metal lines, the variation in the shape of the CDD with impact parameter shows interesting trends as a function of ionisation level. As one moves from impact parameters of 100 kpc to 10 kpc, for lower column density absorbers there is little change in the incidence of absorption. However, as one moves to higher column densities, the number of absorbers increases and the peak moves to higher column densities. The column density where the increase to small impact parameter becomes noticeable increases with ionisation level. For instance, for Mg II the 10 kpc and 100 kpc curves differ at $N_{\rm MgII} \gtrsim 10^{12}\mathrm{cm}^{-2}$, while for C IV they differ at $N_{\rm CIV} \gtrsim 10^{14}\mathrm{cm}^{-2}$. For O VI and Ne VIII, there are only minimal differences in the CDDs at impact parameters of 10 kpc and 100 kpc. At impact parameters of 1 Mpc the number of absorbers is smaller at all columns for all the metal ions, with the peak also generally occurring at lower column densities. The random LOS continue this trend. In short, the lower the ionisation potential, the more sensitive the ion's CDD is to the proximity of a galaxy.

It is conventional to fit the CDD with a power law in column density for a given ion: $f(N) \propto N^{-\beta}$. For random lines of sight, the observed power-law slopes for H I, O VI, and C IV are generally between $1.5 \lesssim \beta \lesssim 2.2$ (Danforth et al. 2006; Cooksey et al. 2010). Davé et al. (2010), using similar simulations, found a slope for the H I CDD of $\beta = 1.70$, which is (unsurprisingly) similar to what we find here. The slope for O VI depends on the range of column densities over which the fit is done, since a pure power law is not a good descriptor. Using the full range above our completeness limit, we obtain $\beta \approx 2.3$, which is comparable to Danforth et al. (2006) who found $\beta = 2.2 \pm 0.1$. C IV likewise is not a perfect power law, but we find a slope of $\beta \approx 1.9$, which is steeper that observations by Cooksey et al. (2010) that yield $\beta = 1.5^{+0.17}_{-0.19}$, but probably within uncertainties given that incompleteness in the data which has poorer quality than our simulated spectra will generically lead to shallower slopes. Given the variations in spectral quality between all these data sets, we consider our simulations to be broadly in agreement with current measures of CDD slopes for these ions. Observations have yet to constrain the slope as a function of impact parameter, but our models predict that the slope does not vary dramatically, and mainly only the amplitude increases substantially to small impact parameter. This prediction will be testable with upcoming observations that have sufficient statistics to examine $f(N)$ as a function of impact parameter.

Looking at the bottom panels of Figure 11, absorption around galaxies in halos of larger and smaller masses continues these same general trends. At impact parameters of 10 kpc, as one goes from halo with masses of $10^{11}M_\odot$ to $10^{13}M_\odot$ one sees similar trends as when one went from impact parameters of 100 kpc to 10 kpc in halos of fixed mass; there is agreement of the CDDs at small column densities and more absorption at high column densities, and the transition occurs at a column density that increases as the ionisation potential of the ion increases. Hence in this regard, going to higher halo masses is equivalent to going to smaller impact parameters in a halo of fixed mass. The CDDs are relatively insensitive to the mass of the galaxy halo for impact parameters of 1 Mpc.

Ne VIII exhibits an interesting trend at high halo masses, arising from its strong collisional ionisation contribution when a hot gaseous atmosphere is present. We see in Figure 5 that Ne VIII has a low-density, photo-ionised component probing the diffuse IGM, which gives it the more extended characteristics of a high ionisation potential ion like O VI that is itself mostly photo-ionised. However, Ne VIII also traces $10^{5.5-6.0}$ K hot halo gas, which is both denser and at lower impact parameters, where cooler ions like Si IV and C IV are also found. Therefore for large halos and impact parameters inside of 100 kpc, there is a substantial population of (collisionally ionised) Ne VIII absorbers. Note that this Ne VIII could be coincident with lower ionisation potential ions, as has been observed by Tripp et al. (2011), but arises in a different gas component.

In summary, the CDD of H I and metal ions shows trends with impact parameter that reflect correlations of absorption with both nearby galaxies and large-scale structure. All ions show increased absorption closer to galaxies. Low ionisation potential ions are more influenced by the presence of nearby galaxies. These CDDs represent a prediction of hierarchical models that enrich the IGM using outflows from star-forming galaxies and can in principle be tested and constrained by observations (e.g., Tumlinson et al. 2011). The full COS-Halos data set is being analyzed now (Werk et al., 2012), and in future work we will undertake a detailed comparison to CDD and other observed statistics, including an artificial spectra sample that more closely mimics the COS-Halos spectra.

7 VARIATIONS WITH OUTFLOW MODEL

One expects the enrichment of the surrounding CGM gas to depend sensitively on the properties of the enriching outflows. So far we have only considered our favoured outflow model with momentum-driven wind scalings. Here we consider how the absorption properties around galaxies depend on our assumed outflow model, using two other wind prescriptions: a simulation with no winds (nw) and a constant wind (cw) model where we assume a constant mass loading factor of $\eta = 2$ and a constant wind speed from all galaxies of $v_w = 680$ km s^{-1}. The latter is similar to that used in the Overwhelmingly Large Simulations (OWLS) reference model of Schaye et al. (2010). The cw version used in this paper is identical to that described in Davé et al. (2010), except that it was re-run using Wiersma et al. (2009a) metal-line cooling rates, for consistency with the vzw model used here.

To begin, Figure 2 shows a pictorial representation of how the physical conditions and absorption vary with wind model. In Figure 12, for easier comparison, we collapse the density and temperature information given in Figure 2 down into one dimension by taking the azimuthal average of those images. In Figure 12, we show a larger region than in Figure 2 to illustrate larger-scale trends, and include metallicity to more fully understand the cooling processes.

In the top panel of Figure 12, vzw curiously shows more similarities to the no wind model (nw) than to the constant wind model (cw). This illustrates that the high wind speeds from all galaxies in the cw model cause significantly more spatial dispersal of mass (along with metals, as we show below) on ∼Mpc scales around galaxies. The vzw model has lower velocity winds that do not have such a dramatic impact on large scales, but do have a strong impact on smaller (CGM) scales. The vzw model pushes more mass via winds into the CGM relative to the no wind model, but this mass is close enough that it recycles back onto the galaxy in much less than a Hubble time (Oppenheimer et al. 2010). We note that the galaxy population is broadly more similar in the two wind models, as they both suppress global star formation substantially relative to the no-wind case (for a fuller discussion of these properties, see Oppenheimer et al. 2010; Davé et al. 2011a,b), but Figure 12 shows that they are quite different in where they deposit the ejected material.

The middle and lower panels of Figure 12 illustrate how winds affect the CGM. Here vzw and cw actually trend in the opposite direction relative to the no-wind case! In the vzw case, the area around the galaxy is slightly colder than with no winds. This is because the lower wind speeds deposit more metals around galaxies (lower panel), and this results in an increased amount of metal cooling (Oppenheimer et al. 2012) that more than offsets the shock heating from the winds. In contrast, the cw model expels gas at high velocities, around the escape velocity for $10^{12} M_\odot$ halos, even from small galaxies. This means the enrichment is more widespread – past 100 kpc, cw shows greater metallicity than the vzw or nw model. Moreover, the wind energy is deposited into less dense gas where it does not have a chance to radiate away its energy.

The H I maps shown in Figure 2 illustrate that winds do not make a large difference to H I absorption, at least on the large scales depicted here, similar to results at high redshift (e.g., Kollmeier et al. 2003; Kollmeier et al. 2006). However, there is an increase in H I on small scales, roughly 100 kpc. The metal absorption, in contrast, shows more dramatic differences between the wind models. In the no-wind case, all the metals are essentially confined to be in and around galaxies, showing that even the distribution of metals within the CGM requires winds. These differences should be manifest in the statistics of absorbers around galaxies, providing an opportunity to constrain wind models.

To further quantify the extent of the metal distribution, Figure 13 shows the fraction of all cosmic metal mass that lies within a given radius from galaxies with $M_* \geqslant 10^{9.1}\ M_\odot$ in the simulation volume. We also plot the fraction of all cosmic mass for all species, in addition to just metals. The procedure for this was discussed in §5. Here the impact of winds on distributing cosmic metals is shown clearly: the no wind model keeps essentially all metals confined very close to galaxies, while the constant wind model disperses them over large scales, with the momentum-driven wind model intermediate between the two. This figure also shows that the constant wind model also pushes the total mass further out, while the momentum-driven wind and no wind models are more similar. For our favoured momentum-driven wind scaling model, 83% of the metal mass is in gas within 300 kpc from galaxies. For the cw model, only 40% is within this radius. Hence the basic extent of metals around galaxies can already provide a discriminant between wind models.

We now aim to quantify these differences in metal distribution using absorption line statistics. Figure 14 is similar

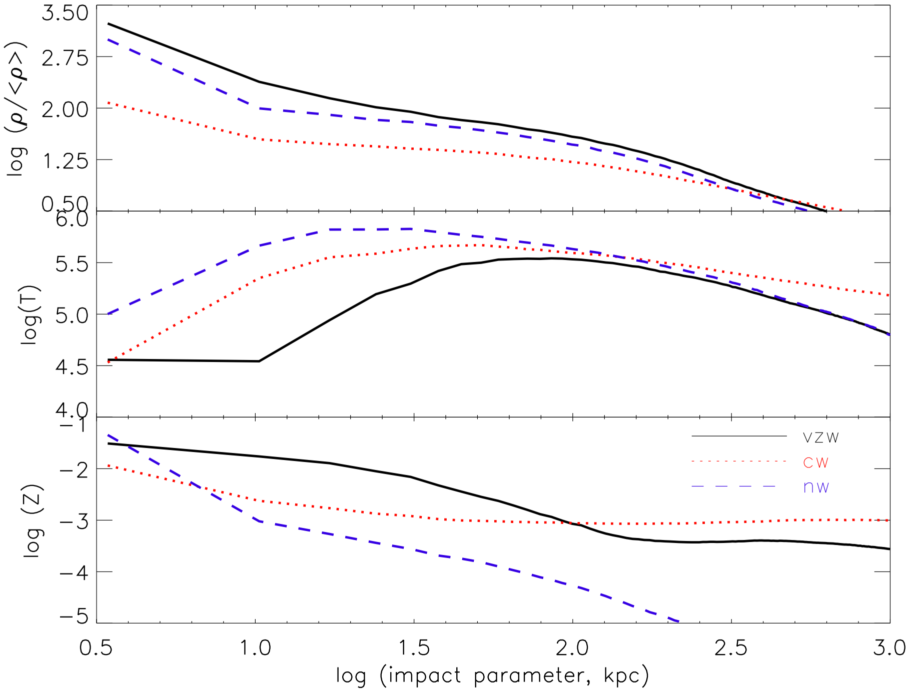

Figure 12. Median overdensity, temperature, and metallicity vs. impact parameter for three different wind models: momentum-driven "vzw", constant wind "cw", and no wind "nw". Sight lines are all around galaxies with halo masses of $10^{12}M_{\odot}$. The top two rows are similar to the first two columns of Figure 2, but collapsing the image down to one dimension.

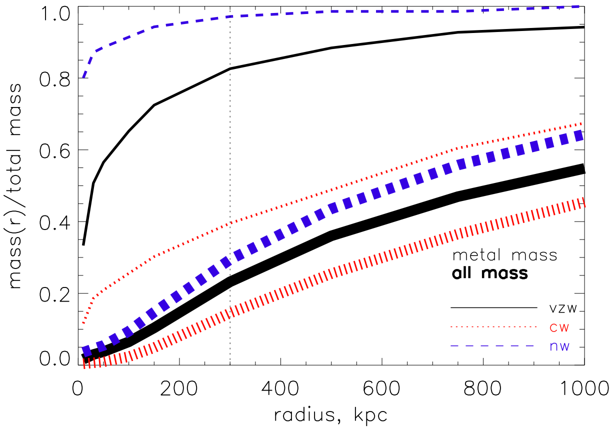

Figure 13. Thin lines: Metal mass fraction of all gas particles within spheres of radius r around all galaxies $M_* \geqslant 10^{9.1}\ M_{\odot}$ in our simulation at z=0.25, relative to the total metal mass of gas particles in the whole simulation volume, for momentum-driven winds (solid line), no winds (dashed line), and constant winds (dotted line). The vertical dotted line delineates 300 kpc. Thick lines: Total mass fraction for all species, not just metals.

to Figure 9, except that it compares the three wind models, using the same column density caps as explained in §3.2. Here, we also include a comparison to our old vzw simulation that used collisionally ionised equilibrium (CIE) metal line cooling, labeled as vzw-cie, as opposed to our current vzw model that uses the Wiersma et al. (2009a) (PIE) cooling. For the most part, the differences between the vzw-cie model and our current vzw model are small compared to the differences between wind models, and hence this aspect of our modeling does not introduce a large uncertainty into the results. The differences between vzw and vzw-cie are small because the winds have moderate velocities, preventing large amounts of gas to reach lower overdensities. Instead, they remain in moderate-density gas where cooling times are short regardless of photo-ionisation suppression. Note that when we generate spectra, we compute ionic abundances including photoionisation in both cases; it is only during the evolution of the simulation that vzw-cie is different.

In this figure, as in Figure 9, we also show dN_{ion}/dz for random LOS for each wind model as the diamonds near the right edge. For all models and ions, dN_{ion}/dz values at 1 Mpc are still higher than dN_{ion}/dz for random LOS. Note that for all the metal ions, there is so little absorption in the no wind model that the random LOS dN_{ion}/dz (purple diamonds) falls off the bottom of this plot. Similarly, the cw model shows so little Si IV and Mg II absorption in random LOS that the red diamonds fall off the bottom of the plot.

For all the metal ions, the no wind model gives significantly less absorption than any of the wind models, even down to the smallest impact parameters probed here. However, there is not a large difference between models with winds and the model without winds for H I. Without outflows, metals basically exist outside the ISM only owing to tidal or ram pressure stripping processes that remove material from the ISM of the central or satellite galaxies.

It is evident from this plot (as with the images in Figure 12) that such stripping processes provide only a small contribution to the CGM metal absorption in these halos, though it can be more substantial in large halos (e.g., Davé, Oppenheimer, & Sivanandam 2008; Zu et al. 2011). Hence, we predict metals seen at any impact parameter beyond that of the ISM of typical galaxies arise almost exclusively owing to outflows.

The differences between the constant wind and momentum-driven wind cases are more subtle. The global trends with ionisation state are as before: lower ionisation potential species are more highly peaked at small impact parameters in both wind models. The main significant difference is an overall offset. In general, the cw model has lower absorption for low ionisation potential species, and higher absorption for high ionisation potential species relative to the vzw (or vzw-cie) model. The lower absorption arises in part because the cw model produces less metals overall owing to its reduced cosmic star formation (Oppenheimer et al. 2012). Going to higher ionisation species, absorption in the cw model becomes only slightly less than absorption in the vzw model. For Ne VIII, cw shows more absorption than vzw. This reflects the impression from Figure 12 that the cw model expels metals to greater distances and heats this diffuse gas more (Oppenheimer et al. 2012). Hence, the global absorption strength as a function of ionisation state provides another potential discriminant between outflow models.

In Figure 15, we plot the median column density versus velocity, analogous to Figure 8 except now we vary the wind model as opposed to the halo mass. Not surprisingly, for H I all the wind models give similar results; however vzw does show an increase over nw and cw at 100 kpc, because these winds push more cool gas to CGM distances. For the metal lines, once again the no-wind case shows virtually no absorption except perhaps very (dynamically) close to galaxies (± 100 km s^{-1}). Hence, tidal effects and other stripping processes are ineffective in distributing metals in velocity space, just as in physical space.

In this figure, we see similar trends with wind model as we did in Figure 14. For low ionisation potential metal species, the vzw model produces higher column densities, while the opposite is true for high ionisation potential species. Previous work (Oppenheimer et al. 2012) has shown that the cw and vzw models enrich the dense gas in quite different ways. The cw model, with its high velocities emanating even from small galaxies, deposits fewer metals into the high density regions very close to galaxies and more metals into the diffuse IGM. Accordingly, metal ions that show more absorption in the cw model than in the vzw model have more absorption from more diffuse IGM gas.

In summary, the rate of the decrease in absorption of metal lines as one moves away from the central galaxy provides a potentially strong discriminant between outflow models that enrich the diffuse IGM to fairly similar levels. Winds are required to enrich the CGM of normal galaxies to any significant level. Our currently favoured momentum-driven wind scaling model predicts more low ionisation potential absorption close to galaxies than the constant wind model and less high ionisation potential absorption farther from galaxies. Quantitative comparisons with present and upcoming COS data should yield more stringent constraints on outflow propagation.

8 CONCLUSIONS

We have examined the absorption line properties of H I and five key metal ions in the vicinity of galaxies at $z = 0.25$ in cosmological hydrodynamic simulations that include galactic outflows, as a function of velocity separation, impact parameter between the galaxy and the line of sight, and halo mass. Our chosen metal ions span a range of ionisation potentials, from low (Mg II) to mid (Si IV & C IV) to high (O VI & Ne VIII). This is the first absorption line study of metal absorption around galaxies in cosmological hydrodynamic simulations with a self-consistently generated outflow model that matches a wide range of galaxy and IGM observables. Our work is motivated by the upcoming wealth of data from *Hubble's* Cosmic Origins Spectrograph, and hence our artificial spectra are generated with resolutions and noise characteristics comparable to the best data that will be obtained with COS.

Our primary conclusions are:

(i) Absorption in all ions is enhanced closer to galaxies. This is true in terms of both impact parameter and velocity separation. A velocity separation of ± 300 km s^{-1} around galaxies encompasses most of the cosmic metal line absorption (although in some cases it can be less), and absorption is also significantly stronger within 300 kpc around a galaxy, particularly for lower ionisation potential lines. These ranges are somewhat larger around bigger galaxies. In our favoured momentum-driven wind simulation, $\approx 80\%$ of all cosmic metals lie within 300 kpc of a galaxy.

(ii) The dependence of metal absorption strength on distance from a galaxy in either physical or redshift space depends monotonically on the ionisation potential of the absorbing ion. Ions with a low ionisation potential (Mg II, Si IV) arise in higher density gas that tends to drop off more quickly with impact parameter and velocity separation than ions with higher ionisation potentials (C IV, O VI, Ne VIII). High ionisation potential absorbers are more associated with gas at halo-like overdensities, and the overall large-scale structure that contains galaxies, while low ionisation potential lines arise more in the dense gas close to individual galaxies. Regardless of ionisation level, even out to 1 Mpc, targeted LOS show an excess of absorption over random LOS, reflective of large-scale matter clustering.

(iii) The majority of cosmic absorption in the ions considered here occurs in photo-ionised gas at $T < 10^5$ K. The exception to this is for the high ionisation lines O VI and Ne VIII at impact parameters $\lesssim 100$ kpc arising in massive halos containing substantial hot gas; these lines are predominantly collisionally ionised.

(iv) The dependence of the column density distributions on impact parameter also shows trends with ionisation potential. Species with lower ionisation potentials are more affected by the proximity of a galaxy. Excepting Ne VIII, our spectra (comparable to COS data quality) directly trace the majority of cosmic absorption; i.e. there is not a large population of smaller absorbers that is inaccessible to COS that would dominate the total cosmic absorption.

(v) Without winds, even gas within ≈ 100 kpc of galaxies remains mostly unenriched; hence outflows are required to enrich the CGM as well as the IGM. The differences in metal absorption between our favoured momentum-driven wind scaling model and a constant wind model are evident

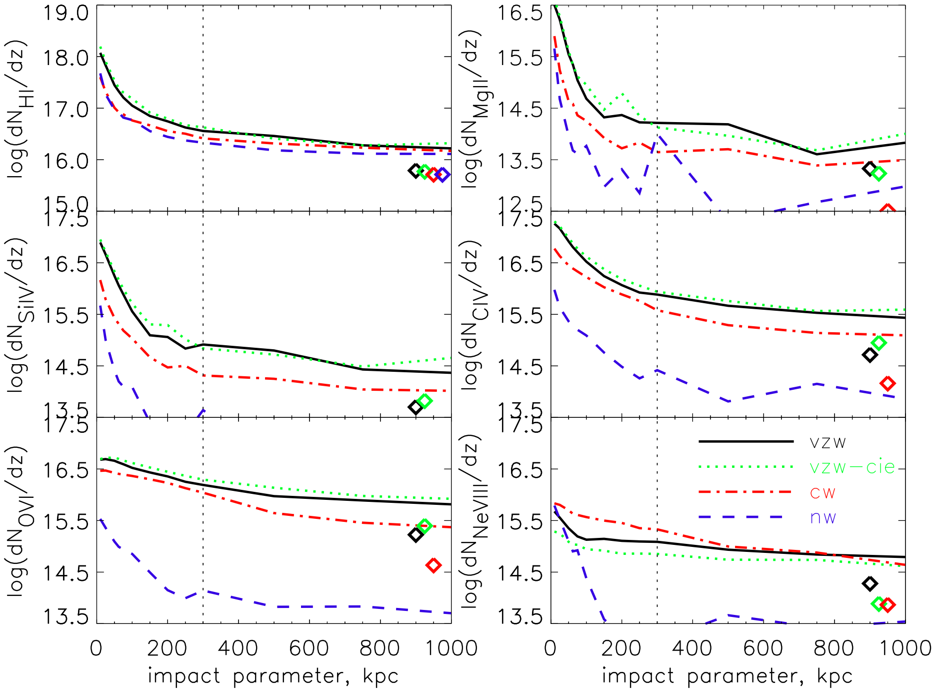

Figure 14. The total column density per unit redshift for the vzw, vzw-cie, cw, and nw models, all for galaxies in $10^{12} M_\odot$ halos. The diamonds indicate the dN_{ion}/dz value for random lines of sight for each wind model. The symbols are shifted slightly to the left of 1 Mpc, and separated for easier viewing. In some cases the symbols are lower than the scale of the plot so do not appear.

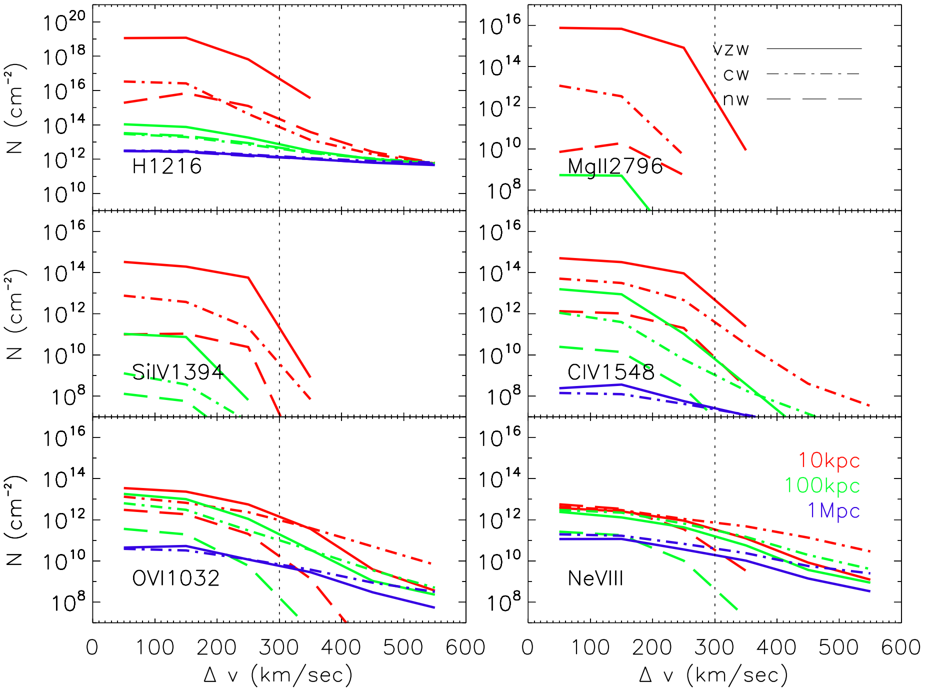

Figure 15. The median column density (N) vs. velocity separation from the central galaxy (Δv) for galaxies in $10^{12} M_\odot$ halos for the vzw, cw, and nw models. We show results at three impact parameters: 10 kpc (red), 100 kpc (green), and 1 Mpc (blue). The vertical dotted marks 300 $\mathrm{km\,s^{-1}}$.

both for lower ionisation potential species close to galaxies and for high ionisation potential species farther from galaxies. The models are clearly distinguishable from each other using the combined CGM statistics of O VI and H I.

These results provide a starting point for understanding how absorption lines trace the metal enrichment around galaxies. We have highlighted some basic trends, and shown that quantifying this distribution as a function of impact parameter and velocity separation can provide interesting constraints on key physical processes such as galactic outflows, as well as the density and temperature state of the metal-enriched IGM.

While we have considered only five metal ions in this paper, the basically monotonic trends with ionisation potential suggest that the behaviour of any other ion can be predicted just based on its ionisation potential. Our simulations predict that higher ionisation potential ions should fall off more slowly at larger impact parameters and velocity separations, because they are tracing lower density, mostly photo-ionised gas. This suggests a physical structure of CGM gas in which O VI is more extended than C IV, which is more extended than Si IV, and so on. Ne VIII and O VI, if probed at sufficiently low column densities, trace the most remote and diffuse metals of any UV resonance line, but their strongest lines arise in hot collisionally ionised gas near large galaxies.

This work is the first step in a series of works to confront successful models for galaxy-IGM coevolution with absorption line observations around galaxies in the low-z universe. We examine redshift $z = 0.25$, but the basic trends are applicable to all redshifts probed by COS ($z \lesssim 1$), as recent work by Davé et al. (2010) and Oppenheimer et al. (2012) show little evolution in the IGM from $z = 1 \rightarrow 0$. We caution, though, that detailed comparisons to observations are premature for the simulated spectra presented here, since quantitative trends can be sensitive to the details of spectral resolution, noise level, etc. Furthermore, our massive galaxies ($M_{\rm halo} = 10^{13}$ M$_\odot$) are all star-forming in these simulations, in clear conflict with observations of mostly passive galaxies in this halo mass range, and hence the predictions for such halos may be influenced by physical effects not included in our current models. Nonetheless, we believe that the basic intuition of understanding metal absorption surrounding galaxies in terms of the ionisation potential of the tracer ion is robust, and provides a clear intuition for interpreting current and future observations. As observations progress, particularly with COS, simulations like these will provide a critical testbed for galaxy formation models, and will help elucidate the physical processes that drive the enrichment of the intergalactic and circumgalactic medium.

9 ACKNOWLEDGEMENTS

We thank Jason Tumlinson, Todd Tripp, Molly Peeples, Joop Schaye, Ben Weiner, Greg Walth, and Greg Stinson for useful discussions. Partial support for this work came from NASA ATP grant NNX10AJ95G, HST grants HST-GO-11598 and HST-GO-12248, NASA ADP grant NNX08AJ44G, and NSF grants AST-0847667, AST-0907998, and AST-133514. The simulations used here were run on the University of Arizona's SGI cluster, ICE, and on computing facilities owned by the Carnegie Observatories. Computing resources used for this work were made possible by a grant from the the Ahmanson foundation, and through grant DMS-0619881 from the National Science Foundation.

REFERENCES

Aguirre, A., Hernquist, L., Schaye, J., et al. 2001a, ApJ, 561, 521
—. 2001b, ApJ, 560, 599
Baldry, I. K., Glazebrook, K., Driver, S. P. 2008, MNRAS, 388, 945
Bell, E. F., McIntosh, D. H., Katz, N., Weinberg, M. D. 2003, ApJ, 585, L117
Blitz, L., & Rosolowsky, E. 2006, ApJ, 650, 933
Bordoloi, R., Lilly, S. J., Knobel, C., et al. 2011, ApJ, 743, 10
Bouche, N., Hohensee, W., Vargas, R., et al. 2012, MNRAS, 426, 801
Bregman, J. N. 2007, ARA&A, 45, 221
Chen, H.-W., Lanzetta, K. M., & Webb, J. K. 2001, ApJ, 556, 158
Chen, H.-W., & Mulchaey, J. S. 2009, ApJ, 701, 1219
Chen, H.-W., Helsby, J. E., Gauthier, J.-R., et al. 2010, ApJ, 714, 1521
Cooksey, K. L., Thom, C., Prochaska, J. X., & Chen, H.-W. 2010, ApJ, 708, 868
Danforth, C. W., Shull, J. M., Rosenberg, J. L., & Stocke, J. T. 2006, ApJ, 640, 716
Danforth, C. W., & Shull, J. M. 2008, ApJ, 679, 194
Davé, R., Hernquist, L., Weinberg, D. H., & Katz, N. 1997, ApJ, 477, 21
Davé, R., Hernquist, L., Katz, N., Weinberg, D. H. 1999, ApJ, 511, 521
Davé, R., Cen, R., Ostriker, J. P., et al. 2001, ApJ, 552, 473
Davé, R., & Oppenheimer, B. D. 2007, MNRAS, 374, 427
Davé, R., Oppenheimer, B. D., Sivanandam, S. 2008, MNRAS, 391, 110
Davé, R., Oppenheimer, B. D., Katz, N., Kollmeier, J. A., & Weinberg, D. H. 2010, MNRAS, 408, 2051
Davé, R., Oppenheimer, B. D., & Finlator, K. 2011a, MNRAS, 415, 11
—. 2011b, MNRAS, 416, 1354
Dekel, A., & Birnboim, Y. 2006, MNRAS, 368, 2
Faucher-Giguère, C.-A., Lidz, A., Zaldarriaga, M., & Hernquist, L. 2009, ApJ, 703, 1416
Ferland, G., Korista, K. T., Verner, D. A., Ferguson, J. W., Kingdon, J. B., Verner, E. M. 1998, PASP, 110, 761
Ferrara, A., Scannapieco, E., Bergeron, J. 2005, ApJL, 634, 37
Finlator, K., Dave, R., Papovich, C., Hernquist,L. ApJ , 639, 672
Finlator, K., & Davé, R. 2008, MNRAS, 385, 2181
Finlator, K., Oppenheimer, B. D., & Davé, R. 2011, MNRAS, 410, 1703
Fumagalli, M., Prochaska, J. X., Kasen, D., et al. 2011, MNRAS, 418, 1796
Gabor, J. M., Davé, R., Oppenheimer, B. D., & Finlator, K. 2011, MNRAS, 417, 2676
Gabor, J. M., & Davé, R. 2012, MNRAS, 427, 1816
Haardt, F., & Madau, P. 2001, in Clusters of Galaxies

and the High Redshift Universe Observed in X-rays, ed. D. M. Neumann & J. T. V. Tran

Hellsten, U., Hernquist, L., Katz, N., & Weinberg, D. H. 1998, ApJ, 499, 172

Hui, L., Gnedin, N. Y., & Zhang, Y. 1997, ApJ, 486, 599

Jarosik, N., Bennett, C. L., Dunkley, J., et al. 2011, ApJS, 192, 14

Kacprzak, G. G., Churchill, C. W., Steidel, C. C., Murphy, M. T., & Evans, J. L. 2007, ApJ, 662, 909

Kacprzak, G. G., Churchill, C. W., Ceverino, D., et al. 2010, ApJ, 711, 533

Katz, N., Weinberg, D. H., & Hernquist, L. 1996, ApJS, 105, 19

Kennicutt, Jr., R. C. 1998, ApJ, 498, 541

Kereš, D., Katz, N., Weinberg, D. H., & Davé, R. 2005, MNRAS, 363, 2

Kollmeier, J. A., Weinberg, D. H., Davé, R. & Katz, N. 2003, ApJ, 594, 75

Kollmeier, J. A., Miralda-Escudé, J., Cen, R., & Ostriker, J. P. 2006, ApJ, 638, 52

Matejek, M. S., & Simcoe, R. A. 2012, ApJ, 761, 112

Ménard, B., Scranton, R., Fukugita, M., & Richards, G. 2010, MNRAS, 405, 1025

McKee, C. F., & Ostriker, J. P. 1977, ApJ, 218, 148

Mulchaey, J. S., & Chen, H.-W. 2009, ApJL, 698, L46

Murray, N., Quataert, E., & Thompson, T. A. 2005, ApJ, 618, 569

Oppenheimer, B. D., & Davé, R. 2006, MNRAS, 373, 1265

—. 2008, MNRAS, 387, 577

—. 2009, MNRAS, 395, 1875

Oppenheimer, B. D., Davé, R., & Finlator, K. 2009, MNRAS, 396, 729

Oppenheimer, B. D., Davé, R., Kereš, D., et al. 2010, MNRAS, 406, 2325

Oppenheimer, B. D., Davé, R., Katz, N., Kollmeier, J. A., & Weinberg, D. H. 2012, MNRAS, 420, 829

Pontzen, A., Governato, F., Pettini, M., et al. 2008, MNRAS, 390, 1349

Prochaska, J. X., Weiner, B., Chen, H.-W., Mulchaey, J., & Cooksey, K. 2011, ApJ, 740, 91

Rubin, K. H. R., Prochaska, J. X., Koo, D. C., & Phillips, A. C. 2012, ApJL, 747, L26

Savage, B. D., Lehner, N., Wakker, B. P., Sembach, K. R., & Tripp, T. M. 2005, ApJ, 626, 776

Schaye, J. 2001, ApJ, 559, 507

Schaye, J., Dalla Vecchia, C., Booth, C. M., et al. 2010, MNRAS, 402, 1536

Schmidt, M. 1959, ApJ, 129, 243

Sembach, K. R., Wakker, B. P., Savage, B. D., et al. 2003, ApJS, 146, 165

Smith, I. W. M. 2011, in IAU Symposium, Vol. 280, IAU Symposium, 361–371

Springel, V. 2005, MNRAS, 364, 1105

Springel, V., & Hernquist, L. 2002, MNRAS, 333, 649

—. 2003, MNRAS, 339, 289

Steidel, C. C., & Sargent, W. L. W. 1992, ApJS, 80, 1

Stinson, G. S., Brook, C., Prochaska, J. X., et al. 2012, MNRAS, 425, 1270

Stocke, J. T., Penton, S. V., Danforth, C. W., et al. 2006, ApJ, 641, 217

Sutherland, R. S., & Dopita, M. A. 1993, ApJS, 88, 253

Tepper-García, T. , Richter, P. Schaye, J., Booth, C. M., Dalla Vecchia, C., Theuns, T., Wiersma, R. P. C. 2011, MNRAS, 413,190

Thom, C., & Chen, H.-W. 2008, ApJL, 683, 22

Tripp, T. M., Savage, B. D., & Jenkins, E. B. 2000, ApJL, 534, L1

Tripp, T. M., Sembach, K. R., Bowen, D. V., et al. 2008, ApJS, 177, 39

Tripp, T. M., Meiring, J. D., Prochaska, J. X., et al. 2011, Science, 334, 952

Tumlinson, J., Thom, C., Werk, J. K., et al. 2011, Science, 334, 948

van de Voort, P. O. 2011, MNRAS, 411, 37

van de Voort, F., Schaye, J., Altay, G., & Theuns, T. 2012, MNRAS, 421, 2809

Wakker, B. P., & Savage, B. D. 2009, ApJS, 182, 378

Wiersma, R. P. C., Schaye, J., & Smith, B. D. 2009a, MNRAS, 393, 99

Wiersma, R. P. C., Schaye, J., Theuns, T., Dalla Vecchia, C., & Tornatore, L. 2009b, MNRAS, 399, 574

Wolfe, A. M., Gawiser, E., & Prochaska, J. X. 2005, ARA&A, 43, 861

Zu, Y., Weinberg, D. H., Davé, R., Fardal, M., Katz, N., Kereš, D., & Oppenheimer, B. D. 2011, MNRAS, 412, 1059